little will be said here. The Gd 4d region is very sensitive to oxidation: note that while the spectrum is broad, oxidation causes a rapid loss in the valley between the two peaks, together with a shift to higher binding energy. Significant changes are seen in the valence band of the pure metal on oxidation, but we do not report the valence band for the films because it will be a complex overlap of the valence band of the component metals and oxides. We recorded the Gd 4d region for all three films but will discuss the data for the aluminum film only. In the silicon/aluminum film the Gd 4d film is complicated by overlap from the Si 2s region, and for the titanium film (which was not depth profiled) little gadolinium intensity was seen. Figure 10 shows how the Gd 4d region changes for the aluminum laser annealed outer layer sample. The two vertical lines indicate the position of metal and oxide peaks. It can be seen that the amount of metal steadily increases with depth profiled. This is indicated by both the increasing amount of the metal component and the increasing valley between the two peaks.

Conclusions

Gadolinium films can be successfully coated with potentially protective films. Laser annealing can alter these protective films and in particular can mix these films with gadolinium to form a gently graded interface. Titanium-protective films appear to lose oxygen to the gadolinium, leading to substantial gadolinium oxidation. It is interesting to note that preferential oxidation of gadolinium has been found in GdFe and GdCo alloy thin films.[21] Aluminum and aluminum/silicon films appear to provide some protection for the gadolinium from oxidation, though some oxidation is found in the X-ray diffraction studies. The nature of the outer oxide layer in the aluminum/silicon evaporated films suggests the formation of aluminosilicates. In the aluminum laser annealed films there is very little metallic aluminum. In both aluminum-containing films the high oxidation of the outer layer seems to correspond to less oxidation and so more protection of the gadolinium inner layer. Some alloying between gadolinium and aluminum is also possible, but we have no direct evidence for alloy formation.

Acknowledgment. We are grateful to the Department of Defense for providing funding for the X-ray diffraction equipment and to Professor Basil Curnutte for assistance with the RBS measurements.

Registry No. Gd, 7440-54-2; Si, 7440-21-3; Al, 7429-90-5; Ti, 7440-32-6.

(19) Wandelt, K.; Brundle, C. R. *Surf. Sci.* **1985**, *157*, 162.
(20) Weller, D.; Sarma, D. D. *Surf. Sci.* **1986**, *171*, L425.
(21) Terzieff, P.; Lee, K. *J. Appl. Phys.* **1979**, *50*, 3565.

Fragment Formalism in Main-Group Solids: Applications to AlB_2, $CaAl_2Si_2$, $BaAl_4$, and Related Materials

Jeremy K. Burdett* and Gordon J. Miller*,†

Department of Chemistry and The James Franck Institute, The University of Chicago, Chicago, Illinois 60637

Received July 10, 1989

Some aspects of the structures of the anion nets in the $CaAl_2Si_2$ and $BaAl_4$ structure types are investigated by using the techniques of tight-binding theory. We examine the factors that stabilize main-group compounds that adopt AlB_2, $CaIn_2$, and $CaAl_2Si_2$ structure types for similar electron counts, i.e., the half-filled band. Traditional molecular orbital concepts and the method of moments are combined to compare the two structural isomers $CaAl_2Si_2$ and $BaAl_4$. Furthermore, we utilize two-dimensional pieces of these two structures as fundamental building blocks to form other main-group compounds.

In recent years the fragment formalism has been widely used to understand and even to predict the structures of inorganic and organometallic molecules, particularly in the area of metallocarboranes. (A recent book that uses this approach to look at a wide range of chemistry is listed in ref 1). The method relies on assembling the orbital picture for a complex system from its constituent fragments, whose structural and electronic characteristics are more easily understood, usually by analogy with simpler systems. To name only one example, the coordination preference for an olefin to an octahedrally based $Fe(CO)_4$ unit is readily clarified by using the frontier orbitals of the two fragments.[2] For extended solids, we have previously shown its utility for examining the electronic factors that control the structural properties of several main-group materials constructed from planar and puckered 6^3 sheets (two-dimensional tessellations of hexagons),[3] as well as the structures of PdXY (XY = P_2, PS, S_2).[4]

In this paper we apply these arguments to structures that contain two prevalent infinite two-dimensional networks:[5] (1) the trigonal $^2_\infty[Al_2Si_2]^{2-}$ bilayer found in $CaAl_2Si_2$;[6] (2) the tetragonal $^2_\infty$[PbO] layer of PbO.[7] Except

†Current address: Max Planck Institut für Festkörperforschung, Heisenbergstrasse 1, 7000 Stuttgart 80, West Germany.

(1) Albright, T. A.; Burdett, J. K.; Whangbo, M.-H. *Orbital Interactions in Chemistry*; Wiley: New York, 1985.
(2) Burdett, J. K. *Molecular Shapes*; Wiley: New York, 1980.
(3) Burdett, J. K. *J. Am. Chem. Soc.* **1980**, *102*, 450.
(4) Burdett, J. K.; Coddens, B. A. *Inorg. Chem.* **1988**, *27*, 418.
(5) Villars, P.; Calvert, L. D. *Pearson's Handbook of Crystallographic Data for Intermetallic Phases*; American Society for Metals: Metals Park, 1985.
(6) Gladyshevskii, E. I.; Kipyakevich, O. I.; Bodak, O. I. *Ukr. Fiz. Zh. (Russ. Ed.)* **1967**, *12*, 447.
(7) Wells, A. F. *Structural Inorganic Chemistry*, 5th ed.; Oxford University Press: London, 1984.

0897-4756/90/2802-0012$02.50/0 © 1990 American Chemical Society

for a few examples, which we discuss later, the trigonal network has been primarily observed in the $CaAl_2Si_2$ structure type. On the other hand, the tetragonal layer is much more prolific. In addition to PbO itself, other structure types that contain this discernable unit include $BaAl_4$,[8] $ThCr_2Si_2$,[9] $CaBe_2Ge_2$,[10] $BaCuSn_2$,[11] and $BaZnBi_2$.[12] (Reference 5 gives an extensive compilation of all compounds adopting these various structure types.) The detailed electronic structures of many of these structure types have been recently described by Hoffmann and colleagues.[13-19] We shall extend their arguments to a fragment orbital approach in order to consider many different structural possibilities that may occur when solids are constructed from these two networks. Our qualitative arguments are supplemented by quantitative results obtained by using the extended Hückel theory within the framework of the tight-binding approximation.[20] Details of the computations are presented in the Appendix.

In 1 and 2, respectively, we show the fundamental networks for $^2_\infty[Al_2Si_2]^{2-}$ and $^2_\infty[PbO]$. In each layer, every

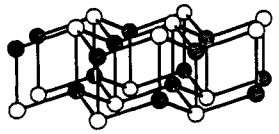

1

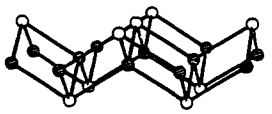

2

atom is four-coordinate—the shaded atoms are tetrahedrally coordinated, albeit slightly distorted (Al in $^2_\infty[Al_2Si_2]^{2-}$ has 3m (C_{3v}) site symmetry, and O in PbO has $\bar{4}2m$ (D_{2d}) site symmetry), whereas the unshaded atoms each have an unusual asymmetric environment for main-group atoms. For $^2_\infty[Al_2Si_2]^{2-}$ the local coordination at each Si atom may be described as an "inverted tetrahedron" or an "umbrella", which is similar to the sulfur coordination in sulvanite, Cu_3VS_4.[21] In PbO each Pb atom occupies the apex of a square pyramid. These two local geometries are illustrated in 3.

3

If we appeal to traditional ways of describing solid-state structures, i.e., in terms of sphere packings, we see that $CaAl_2Si_2$ represents hexagonally close-packed Si atoms with an ordered arrangement of Ca atoms in one-half of the octahedral holes and Al in one-half of the tetrahedral holes. In this way, $CaAl_2Si_2$ is a ternary variant of the La_2O_3 structure ($La_2O_3 \equiv O^{oct}O^{tet}{}_2La_2$).[22] PbO represents

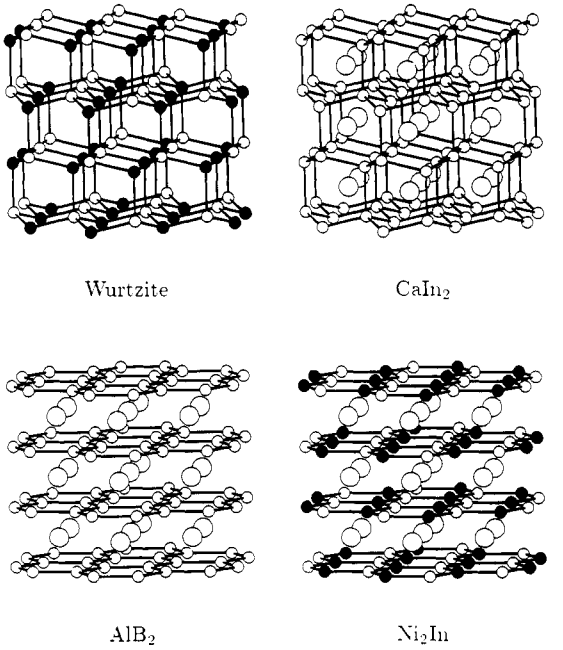

Figure 1. Various structure types containing 6^3 nets stacked in an eclipsed configuration. Beginning top left and proceeding clockwise: (1) wurtzite; (2) $CaIn_2$; (3) Ni_2In; (4) AlB_2.

a tetragonal variant of a cubic closest packing of atoms. The lower symmetry derives from the particular coloring of the fcc arrangement, as well as from the lattice parameters. The c/a ratios in PbO, SnO, FeSe, and FeTe[5] indicate that they are definitely layer structures, whereas InBi is much less so.[22]

We have organized this article by first developing the trigonal $^2_\infty[Al_2Si_2]^{2-}$ bilayer as a fragment derived from a three-dimensional solid—the AlB_2-type structure. This treatment allows us to examine other related distortion coordinates of the AlB_2 framework as well. After this we compare the $^2_\infty[Al_2Si_2]$ and $^2_\infty[PbO]$ layers energetically and, finally, present a number of examples in which these fragments are used to form other diverse types of inorganic main-group structure types.

Stacking of 6^3 Nets

Another description of the $^2_\infty[AlSi]^-$ 6^3 sheets to form Al–Si linkages between the layers. (Eclipsed stacking of 6^3 nets forms hexagonal channels along **c**.) In the complete structure these bilayers are themselves stacked in an eclipsed fashion, although the Ca atoms maintain extended Al–Si distances between adjacent bilayers. This stacking mode of puckered or planar 6^3 nets, both with and without interlayer connections, occurs in a number of main-group structures, some of which include wurtzite (ZnS), AlB_2-type, Ni_2In-type, and $CaIn_2$ (see Figure 1).[5] The AlB_2-type ($P6/mmm$) and Ni_2In-type ($P6_3/mmc$) structures are class-equivalent but not lattice-equivalent since $\mathbf{c}(Ni_2In) = 2\mathbf{c}(AlB_2)$. In ternary variants of the AlB_2 type, the elements that occupy the 2nd sites (the B positions in AlB_2) must be randomly distributed in order to account for the lattice parameters and translational symmetry. In addition, we see from the figure that the $CaIn_2$ structure may be described either as stuffed wurtzite or as a puckering of AlB_2.

Except for wurtzite-type structures, all other compounds contain electropositive elements in the hexagonal prismatic holes between the sheets (n.b., in $CaIn_2$ this site may be better described as the center of two interpenetrating trigonal prisms). If we restrict our attention to those compounds in which the nets are formed from elements

(8) Andress, K. R.; Alberti, E. *Z. Metallkde.* **1935**, *27*, 126.
(9) Ban, Z.; Sikirica, M. *Acta Crystallogr.* **1965**, *18*, 594.
(10) Eisenmann, B.; May, N.; Müller, W.; Schäfer, H. *Z. Naturforsch., Teil B* **1972**, *27*, 1155.
(11) May, N.; Schäfer, H. *Z. Naturforsch., Teil B* **1974**, *29*, 20.
(12) Cordier, G.; Eisenmann, B.; Schäfer, H. *Z. Anorg. Allg. Chem.* **1976**, *426*, 205.
(13) Zheng, C.; Hoffmann, R. *Z. Naturforsch., Teil B* **1986**, *41*, 292.
(14) Zheng, C.; Hoffmann, R.; Nesper, R.; von Schnering, H. G. *J. Am. Chem. Soc.* **1986**, *108*, 1876.
(15) Hoffmann, R.; Zheng, C. *J. Phys. Chem.* **1985**, *89*, 4175.
(16) Zheng, C.; Hoffmann, R. *J. Solid State Chem.* **1988**, *72*, 58.
(17) Zheng, C.; Hoffmann, R. *J. Am. Chem. Soc.* **1986**, *108*, 3078.
(18) Ramirez, R.; Nesper, R.; von Schnering, H. G.; Böhm, M. C. *Z. Naturforsch, Teil A* **1987**, *42*, 670.
(19) Trinquier, G.; Hoffmann, R. *J. Phys. Chem.* **1984**, *88*, 6696.
(20) (a) Hoffmann, R. *J. Chem. Phys.* **1963**, *39*, 1397. (b) Ammeter, J.; Bürgi, H.-B.; Thibeault, J. C.; Hoffmann, R. *J. Am. Chem. Soc.* **1978**, *100*, 3686.
(21) Trojer, F. J. *Am. Mineral.* **1966**, *51*, 890.
(22) Pearson, W. B. *Crystal Chemistry and Physics of Metals and Alloys*; Wiley: New York, 1972.

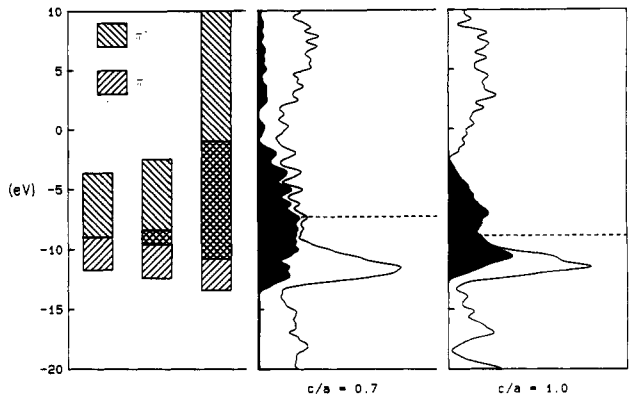

Figure 2. Projection of π and π^* bands from the DOS of an AlB_2 framework with c/a ratios 0.7 and 1.0. On the left, the three blocks represent the p_z projections when c/a is infinite, 1.0, and 0.7, respectively. The cross-hatched region indicates overlapping of π and π^* orbitals.

in groups 11–16 and the inserted atoms are alkali, alkaline-earth, or rare-metals, then in the spirit of the Zintl–Klemm–Busmann rules,[23] we can consider these "cations" to simply donate their electrons to the "anion framework". Each of these structure types occur within a narrow range of valence electron concentration that averages nearly four electrons per anionic constituent. If we include the $CaAl_2Si_2$ structure type in these classes of compounds, then we obtain three primary structural groups: (1) planar 6^3 monolayers as in AlB_2- or Ni_2In-type compounds; (2) puckered 6^3 sheets in wurtzite-, $CaIn_2$-, or LiGaGe-type compounds; (3) puckered 6^3 bilayers found in $CaAl_2Si_2$- or Mg_3Bi_2-type materials. We shall now examine the factors that influence which structure is preferred in this isoelectronic family.

We begin with, perhaps, the simplest and, certainly, most symmetrical example: the monatomic anion network in the AlB_2-type structure.[24] Figure 2 illustrates the π_z and π^*_z projections from the total DOS for two examples (using Si as the atom of choice) with c/a ratios of 0.7 and 1.0. In an isolated 6^3 net of Si atoms, translational symmetry dictates that at the point K ($=^1/_3\mathbf{k}_1 + ^1/_3\mathbf{k}_2$) in the hexagonal Brillouin zone, the π and π^* bands will just touch to give zero density of states (DOS) at the Fermi level for the half-filled band.[25] In other words, the π bonding in this honeycomb net is maximized for four electrons per atom.[26] The most significant interactions between adjacent sheets occur via σ_p overlap of these π and π^* bands—the frontier orbitals of the graphite-type sheet. Thus, as Figure 2 indicates, weak σ_p interactions between the 6^3 sheets (c/a = 1.0) effect only a small overlap in energy of the π and π^* bands, which then produces a nonzero DOS at the Fermi level. Recent studies suggest that these orbital overlaps between the sheets account for the electrical conductivity in the novel layer phase BC_3, since calculations on the isolated two-dimensional net is predicted to be semiconducting (energy gaps $\sim$1 eV).[27] As these honeycomb nets are brought even closer together (c/a = 0.7), the interplane σ_p overlap begins to dominate and eventually leads to a substantial occupation of the equatorial π^* component. Previous examination of the electronic structure of As and isoelectronic phases with five valence electrons per atom show that the observed puckering of the 6^3 nets greatly stabilizes the occupied π^* band.[28] The molecular analogue is the observed pyramidal C_{3v} geometry of NH_3, as opposed to a planar D_{3h} structure, e.g., in BH_3.[2] Therefore, we anticipate the AlB_2 framework with relatively short interlayer distances to be unstable with respect to puckering of each 6^3 net for the half-filled band case, as the intraplane π^* band becomes increasingly populated.

The following questions arise: (1) how close should these hexagonal sheets approach each other before a puckering distortion stabilizes the structure; (2) when a puckering distortion is anticipated, what sort of geometrical distortion should occur; (3) what is the effect of stoichiometry on the observed distortion coordinate? Table I lists a normalized c/a ratio for a number of different structures that show

Table I. Compounds Adopting AlB_2- or $CaIn_2$-Type Structure[5]

compd	c/a	compd	c/a
AlB_2		$CaIn_2$	
MgB_2	1.142	$BaTl_2$	0.808
$EuGa_2$	1.040	$CaGa_2$	0.825
$SrGa_2$	1.089	$CaIn_2$	0.792
BaBeSi	1.247	$EuIn_2$	0.791
BaZnSi	1.103	$EuTl_2$	0.791
DyCuSi	0.966	$MgGa_2$	0.804
DyCuGe	0.868	$YbGa_2$	0.806
GdCuSi	0.996	$SrIn_2$	0.802
GdCuGe	0.898	$YbIn_2$	0.780
LaCuGe	0.937	$SrTl_2$	0.810
LaCuSn	0.891	GdCuSn	0.813
PrCuSi	1.009	GdCuPb	0.808
Ni_2In		TbCuSn	0.808
BaCuAs	1.038	DyZnIn	0.779
CaCuAs	0.940	DyZnTl	0.792
KZnAs	1.210	GdZnIn	0.784
NaBeSb	1.125	GdZnTl	0.796
CaCuBi	0.892	LaZnIn	0.810
SrZnSi	1.049	YbZnIn	0.781
DyCuSi	0.895	LiGaGe	
DyCuSn	0.810	LiBeSb	0.811
EuCuP	0.995	LiZnBi	0.806
LaCuSi	0.956	LiGaGe	0.812
PrCuSi	0.937	LiGaSi	0.808
KZnP	1.240	LiZnSb	0.808

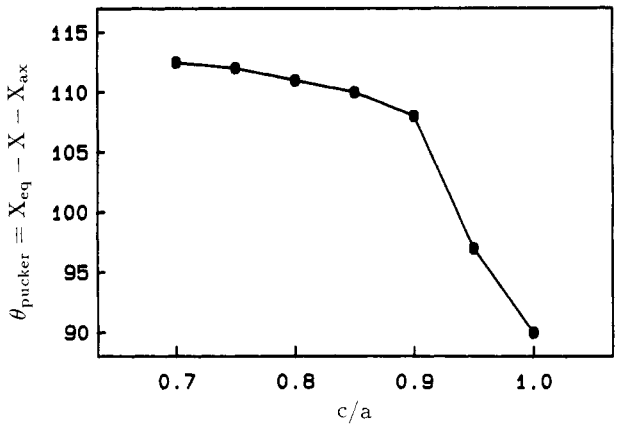

Figure 3. Puckering angle of each 6^3 sheet that minimizes the total energy of an eclipsed stacking configuration of 6^3 nets as a function of c/a. For a given c/a value, θ_{pucker} was determined for structures at constant volume.

(23) Schäfer, H.; Eisenmann, B.; Müller, W. *Angew. Chem., Int. Ed. Engl.* **1973**, *12*, 694.
(24) Burdett, J. K.; Canadell, E.; Miller, G. J. *J. Am. Chem. Soc.* **1986**, *108*, 6561.
(25) Whangbo, M.-H.; Hoffmann, R.; Woodward, R. B. *Proc. R. Soc. London, Ser. A* **1979**, *366*, 23.
(26) Zheng, C.; Hoffmann, R. *Inorg. Chem.* **1989**, *28*, 1074.
(27) (a) Kouvetakis, J.; Kaner, R. B.; Sattler, M. L.; Bartlett, N. *J. Chem. Soc., D Chem. Commun.* **1986**, 1758. (b) Tománek, D.; Wentzcovitch, R. M.; Louie, S. G.; Cohen, M. L. *Phys. Rev. B* **1988**, *37*, 3134. (c) Lee, Y.-S.; Kertesz, M. *J. Chem. Soc. D, Chem. Commun.* **1988**, 75. (d) Wentzcovitch, R. M.; Cohen, M. L.; Louie, S. G.; Tománek, D. *Solid State Commun.* **1988**, *67*, 515.
(28) Burdett, J. K.; Lin, J.-H. *Acta Crystallogr., Sect. B* **1981**, *37*, 2123.

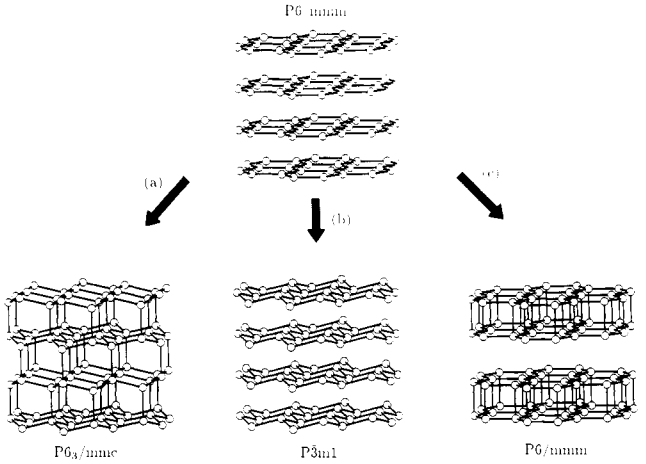

Figure 4. Three possible distortion modes of the AlB_2 framework that maintain the same a_1 and a_2. From left to right: (a) $P6/mmm \rightarrow P6_3/mmc$; (b) $P6/mmm \rightarrow P\bar{3}m1$; (c) $P6/mmm \rightarrow P6/mmm$ ($\mathbf{c} \rightarrow 2\mathbf{c}$).

eclipsed stacking of 6^3 nets. The normalization of the c/a ratio is with respect to the AlB_2-type geometry. With very few exceptions, the AlB_2- and Ni_2In-type structures are found for a value greater than $\sim$0.85, while $CaIn_2$- and LiGaGe-type structures have a ratio less than 0.85.[5] Figure 3 plots the X_{eq}–X–X_{ax} angle (=90° for AlB_2 and $\sim$109.5° for $CaIn_2$) that minimizes the total energy of the monatomic network as a function of c/a. These total energy calculations were performed on a Si structure at constant volume for a given c/a ratio with the puckering of the 6^3 sheets proceeding toward the wurtzite geometry. Given the problem of trying to optimize internuclear separations by using the extended Hückel method, it is not surprising that we should predict c/a ratio of approximately 0.95, at which puckering of the 6^3 nets should commence. Nevertheless, since we are attempting to account for a large amount of structural observations using a single system, the trend is clear: the smaller the c/a ratio, the greater is the tendency to pucker the 6^3 sheets. Furthermore, the puckering angle that minimizes the total energy increases with decreasing c/a. Not much structural data are yet available to test this conclusion.

The particular distortion examined in Figure 3, that between AlB_2 and $CaIn_2$ structure types, is only one of many conceivable geometrical changes that introduce puckering of the planar 6^3 nets. With respect to the second question raised above, we shall limit attention to those geometrical perturbations that retain at least the trigonal axis and leave a_1 (AlB_2) and a_2 (AlB_2) unaltered. Three obvious distortion modes are illustrated in Figure 4. In addition to the $AlB_2 \rightarrow CaIn_2$ transformation (a, $P6/mmm \rightarrow P6_3/mmc$), the other two show a coherent puckering of each 6^3 sheet (b, $P6/mmm \rightarrow P\bar{3}m1$) and a doubled graphite stacking (c, $P6/mmm \rightarrow P6/mmm$), respectively. Although this last distortion does not involve puckering of the individual sheets, it is an intermediate step toward the $^2_\infty[Al_2Si_2)]^{2-}$ bilayer. Structures that result from distortion (b) occur in $EuGe_2$ and MCd_2 compounds (M = lanthanide) for electron counts either less than or greater than four per main-group atom.[5] We should also note that distortions (a) and (c) transform $\mathbf{c}(AlB_2)$ to $2\mathbf{c}$ via bond-length alternation along the **c** axis, whereas distortion (b) leaves $\mathbf{c}(AlB_2)$ unchanged. To probe which distortion coordinate leads to greater electronic stability, we illustrate in Figure 5 the electronic energy bands along selected directions in the hexagonal Brillouin zone for the AlB_2 structure with a c/a ratio of 1.0, i.e., at the point just above

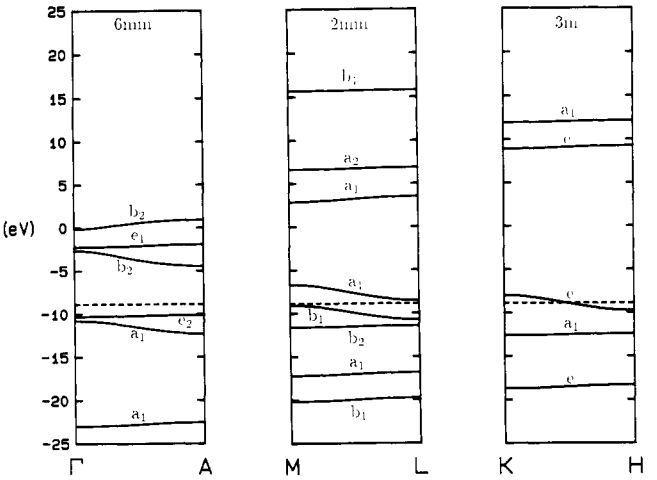

Figure 5. Energy band dispersion curves for the AlB_2 framework (c/a = 1.0) along the three high-symmetry directions parallel to **c*** in the hexagonal Brillouin zone: (left) ΓA; (middle) ML; (right) KH. The dashed line indicates the calculated Fermi level for four electrons per atom.

the extended Hückel prediction for distortion to the $CaIn_2$ structure. Unlike the isolated two-dimensional graphite-type case, the Fermi level for four electrons per atom falls just below the degeneracy in the π–π^* band at K. In fact, the Fermi level cuts a doubly degenerate band along the line KH at $k_z = \pi/2c$ and does not pass through any other bands along the other vertical directions, including both ΓA and LM. Due to the relatively large interlayer separation and concomitant weak orbital overlap, the energy band dispersion parallel to **c*** is much smaller than that perpendicular to **c***. As expected, the bands that show the greatest dispersion along directions parallel to **c*** are the frontier orbitals of the 6^3 sheet—the π and π^* bands. Both of these bands decrease in energy from $k_z = 0$ to $k_z = \pi/c$ due to the nature of the p_z overlap and the phase changes associated with the two planes in reciprocal space, **4**.

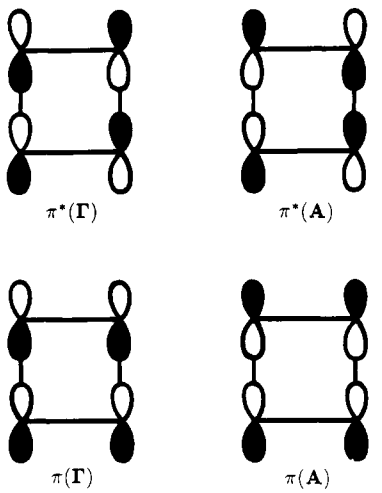

4

According to the tight-binding formalism with only nearest-neighbor interactions included, an analytical expression can be written for the energies of the π and π^* bands in reciprocal space:[29]

$$E_\pi(\mathbf{k}) = \beta\{3 + 2[\cos(\mathbf{k}\cdot a_1) + \cos(\mathbf{k}\cdot a_2) + \cos(\mathbf{k}\cdot(a_1 + a_2))]\}^{1/2} + 2\beta' \cos(\mathbf{k}\cdot\mathbf{c})$$

in which $\beta(=\beta_\pi) < 0$ and $\beta'(=\beta_{p\sigma}) > 0$. When we substitute

(29) Burdett, J. K. *Prog. Solid State Chem.* **1984**, *15*, 173.

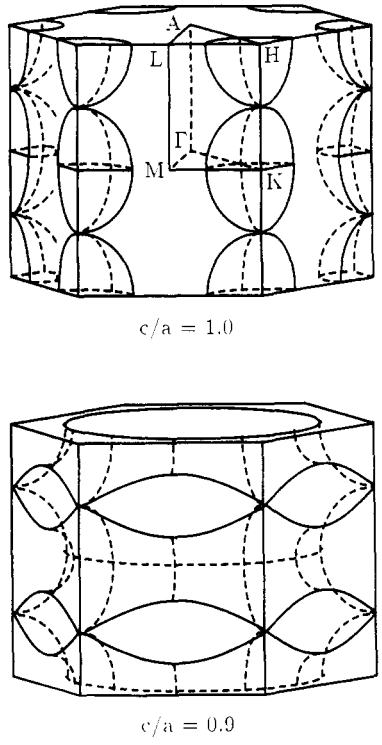

Figure 6. Fermi surfaces for the AlB_2 framework with c/a ratios of 1.0 (top) and 0.9 (bottom) for four electrons per atom. Solid lines occur on the surface of the hexagonal prism, while dashed lines are inside the polyhedra. For c/a = 1.0, the ellipsoids centered at K enclose holes, and those centered at H enclose electrons. Upon compression of the structure, these ellipsoids transform into toroids at c/a = 0.9.

the appropriate values of **k** into this expression, we obtain the following dispersion relations for the three lines parallel to **c***:

$$E(\Gamma A) = \pm 3\beta + 2\beta' \cos(k_z c)$$

$$E(ML) = \pm \beta + 2\beta' \cos(k_z c)$$

$$E(KH) = 2\beta' \cos(k_z c)\ (2\times)$$

In this simple model, E(KH) is a doubly degenerate band. In this simple model, we have neglected the symmetry-allowed mixing between s orbitals and the π/π^* bands because this primarily affects the position of the band centers and not their dispersion characteristics (Note: this mixing may not occur at $k_z = 0$ or $k_z = \pi/c$ due to the horizontal mirror planes that are contained in the group of **k** with this k_z component.)

If we consider the degenerate band along KH and the intersection of the Fermi energy at its midpoint, the electronic situation, therefore, suggests susceptibility towards a Peierl's distortion along the **c** axis.[30] And yet, for large c/a ratios, the structure does not distort. Apparently, the strength of the π interactions within the 6^3 sheets is sufficient to maintain the AlB_2 geometry. As the 6^3 sheets are brought closer together, i.e., to give c/a ratios less than 1.0, the most dramatic changes occur first along the ML line. Using the expression for the dispersion curve for E(ML) in conjunction with Figure 5, the top of the π-bonding band at M is pushed above the Fermi level due to σ^*_p overlap between the pπ orbitals, while at L, the bottom of the π^* band drops below E_F. Rather than illustrate several band structure diagrams for various c/a ratios, Figure 6 shows the evolution of the Fermi surface (that region in reciprocal space that separates occupied from unoccupied states) for the two cases, c/a = 1.0 and c/a = 0.9, with four electrons per "anion". The ellipsoids (c/a = 1.0) and toroids (c/a = 0.9) centered at K enclose holes, while those centered at H enclose electrons. For moderate compression of the **c** axis, the Fermi level still intersects the KH line near the midpoint of a doubly degenerate band and nesting of the Fermi surfaces remains. Puckering distortions that break the degeneracy at the midpoint of KH will lead to the greatest stabilization of the AlB_2 framework. Given the tight-binding expressions for $E(\mathbf{k})$ and the results from Figures 3 and 5, we first observe puckering when $\beta \sim 2\beta'$, or, from the Wolfsberg–Helmholz expression ($\beta \propto S$), when $S_{p\sigma} \sim {}^1/_2 S_{p\pi}$.

Therefore, the $CaIn_2$ structure is a manifestation of the Peierl's instability associated with an axially compressed AlB_2 structure. The puckering is further enhanced via second-order mixing of the π-bonding band with the σ^*_s band. Unlike its molecular analogue, i.e., the C_{3v} point symmetry of NH_3, which may be understood via second-order Jahn–Teller arguments,[1,2] this distortion should be attributed to first-order changes in the total energy surface. Furthermore, we may conclude that a transformation of type (c) will also stabilize the AlB_2 framework for sufficiently strong intersheet interactions, simply by removing the 6_3 screw axis. For the monatomic network, the moments method[31] can now be applied to understand which of the two distortion coordinates is preferred. At the half-filled band, six-membered rings within a structure are energetically more favorable than four-membered rings. The transformation from an axially compressed AlB_2 network to the $CaIn_2$-type structure introduces only six-membered rings into the main group net, whereas the transformation (c) forms only four-atom cycles. However, these four-membered rings may be stabilized by alternately coloring the vertices with atoms of two different electronegativities. In fact, at the half-filled point, completely alternant systems are energetically preferred. For the cases listed in Table I, every binary network is indeed alternant, except for the ternary examples of the AlB_2 type in which, by symmetry, there must be a statistical 50%–50% occupation of the 2d sites by the two different atoms.

In the alternant system, the degeneracy in the π–π^* band is broken along KH, and an energy gap persists throughout the Brillouin zone for the half-filled case (four electrons per atom). This broken degeneracy removes the Peierl's instability in the three-dimensional structure, and yet geometrical distortions similar to those between AlB_2 and $CaIn_2$ are observed. The coloring pattern of the main-group framework of AlB_2 changes the space group to $P6_3/mmc$ (**c** → 2**c**), and we now use Ni_2In as the prototype. Figure 7 shows two energy band dispersion curves along ΓA for two different c/a ratios in a $^3_\infty$[AlSi] framework: (a) $c/a > 1.50$; (b) $c/a < 1.50$. Calculations on this network using 2.45 Å as the Al–Si distance within each 6^3 net indicate that a Ni_2In → LiGaGe transition ($P6_3/mmc$ → $P6_3mc$) occurs for $c/a \sim 1.5$ (this value corresponds to 0.75 in Table I; again we cite the sensitivity of this result to the parameters we have selected—recall for the monatomic net, we obtained a critical value of 0.85). The dashed lines indicate the expected dispersion when the symmetry imposed avoided crossings are neglected. For c/a ratios greater than 1.5, the bands separate into predominantly σ_s and π below the Fermi level and π^* and σ^*_s above the Fermi level. Weak interactions between adjacent planes produce small band widths and a relatively large energy

(30) Peierls, R. *Quantum Theory of Solids*; Oxford University Press: Oxford, 1955.

(31) Burdett, J. K.; Lee, S. J. *J. Am. Chem. Soc.* **1987**, *107*, 3050.

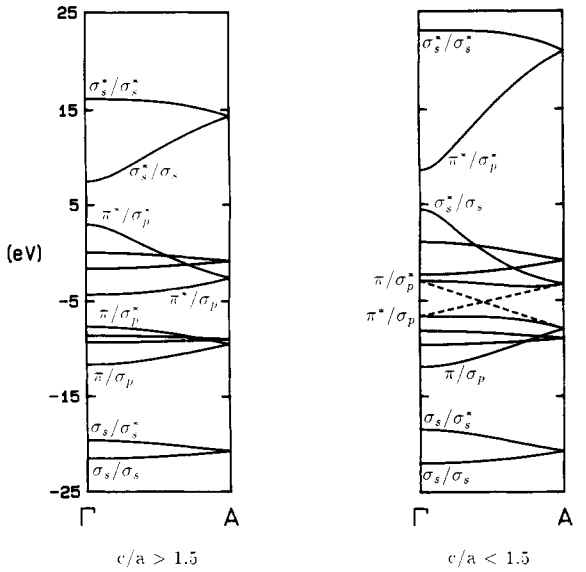

Figure 7. Energy band dispersion curves along ΓA for two geometrical conditions in a completely alternant $^3_\infty$[AlSi] network with planar 6^3 nets: (left) $c/a > 1.5$; (right) $c/a < 1.5$. For the compressed structure, avoided crossings are indicated by the dashed lines. Only s and p bands are included.

separation between π and π^* bands. Therefore, no distortion is expected for this geometrical condition.

For c/a ratios less than 1.5, there exist substantial differences among crystal orbitals near the Fermi energy from those of case (a). The changes occur abruptly as c/a is reduced due to an avoided crossing **5**, which still main-

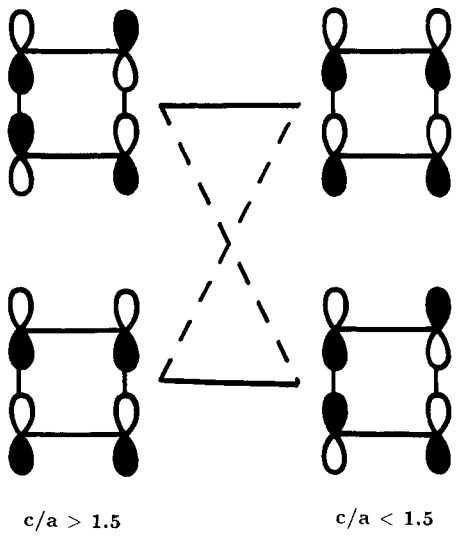

5

tains the energy gap between the valence and conduction bands. Under the space group $P6_3/mmc$, the interplanar σ_p combination of an intraplanar π^* band transforms according to the same irreducible representation at Γ as the σ^*_p combination of a π band. As the σ_p overlap between adjacent π or π^* bands increases, we now find a π^* band below and a corresponding π band above the Fermi level. At the critical point, $c/a \sim 1.5$, we also calculate the smallest energy gap between occupied and unoccupied energy bands (n.b., although we illustrate bands only along ΓA, we find the smallest optical gap, $\Delta\mathbf{k} = 0$, at the point $H = (^1/_3,^1/_3,^1/_3)$, $E_g = 2.47$ eV). How can we understand the observed distortions of this alternant framework given these computational results?

In the study of molecular structures, the second-order Jahn–Teller approach provides a method for determining the symmetry of the distortion coordinate that will mix together HOMO and LUMO so as to stabilize the molecule, e.g., the NH_3 problem.[2] After some manipulation of the Hamiltonian, the energy of a system that is distorted within the coordinate u_i may be written as[2]

$$E(u_i) = E_0 + u_i\langle\Psi_0|H_i|\Psi_0\rangle + \tfrac{1}{2}u_i^2\left[\langle\Psi_0|H_{ii}|\Psi_0\rangle + 2\sum_{m\neq 0}\frac{|\langle\Psi_0|H_i|\Psi_m\rangle|^2}{E_0^{(0)} - E_m^{(0)}}\right] + \cdots$$

in which $\Psi_0, E_0^{(0)}$ and $\Psi_m, E_m^{(0)}$ are the ground-state and excited-state wave functions and energies, respectively (therefore, $E_0^{(0)} < E_m^{(0)}$). The second term in the expansion is the first-order Jahn–Teller term and is effective only when Ψ_0 is orbitally degenerate. The second-order Jahn–Teller effect is assigned to the third term. The force constant for distortion within the coordinate u_i consists of two contributions: (1) a "classical" force constant, which represents nuclear motion in a static electronic distribution; (2) a relaxation term that describes the energy change of the electron distribution as it "follows" the nuclei. When this term is negative, the system will spontaneously distort until it reaches a relative minimum on the potential surface. It signs depends upon the size of the energy difference, $E_0^{(0)} - E_m^{(0)}$, and whether the integral $\langle\Psi_0|H_i|\Psi_m\rangle$ is nonzero. This integral will be nonzero only if the irreducible representation assigned to the distortion coordinate u_i is contained within the direct product of the two wave functions, $\Psi_0 \otimes \Psi_m$. To apply this concept to crystalline solids, the Bloch theorem requires that $\mathbf{k}_0 + \mathbf{k}(u_i) - \mathbf{k}_m = 0$ in order for the interaction integral to be nonzero. If we consider only direct transitions, i.e., $\mathbf{k}_0 = \mathbf{k}_m$, then we search for the appropriate phonon mode with wave vector $\mathbf{k}(u_i) = 0$.

The group of the wave vector along ΓA for Ni_2In is isomorphous to 6mm (C_{6v}). The bands assigned to the s and p_z orbitals on each constituent are labeled as either a_1 or b_1 in this group. Therefore, under the ideas of the second-order Jahn–Teller effect, only vibrations (or phonons in this case) that transform as a_1 or b_1 will couple the valence and conduction bands and lead to distortion of the structure. The four normal modes along the **c** axis are diagrammed in **6**, and all are Jahn–Teller-allowed vibra-

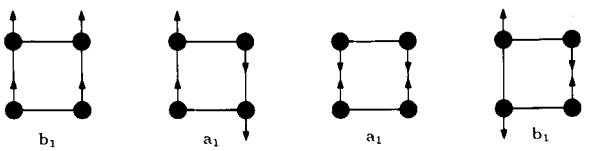

6

tional modes. One corresponds to an acoustic mode ($a\ b_1$ mode). The a_1 distortions do not remove the inversion center in $P6_3/mmc$ and lead to the bilayer structure ($P6_3/mmc \rightarrow P\bar{3}m1$), while the b_1 distortion eliminates the inversion operation but retains the 6_3 screw axis ($P6_3/mmc \rightarrow P6_3mc$). Again, we can appeal to the moments method to determine the preferred distortion coordinate—that toward the wurtzite-type geometry, i.e., a b_1-type perturbation. However, we shall see shortly that the bilayer structure may occur under specific stoichiometric conditions.

Before we address this problem, can we envision a physically induced transformation from N_2In-type to LiGaGe-type structures? Scheme **5** and Figure 7 indicate that as the Ni_2In structure is compressed along the **c** axis, the concerted transformation, $P6_3/mmc \rightarrow P6_3mc$, is a thermally forbidden process due to the crossing of π and π^* bands, according to the ideas of Burdett and Price

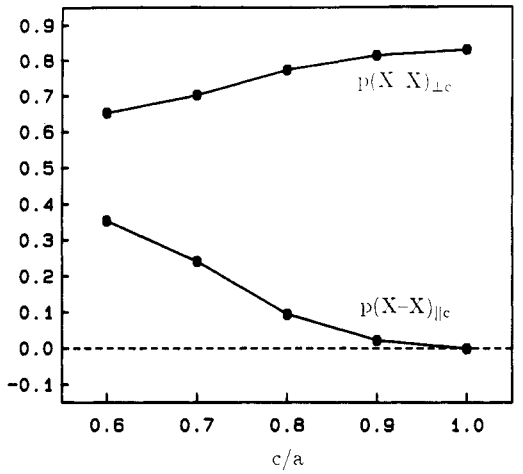

Figure 8. Overlap populations between and within each 6^3 net in the AlB_2 structure as a function of c/a. Throughout the observed range, $p(X\text{-}X)_{\perp c} > p(X\text{-}X)_{\parallel c}$.

concerning solid-state polymorphic-phase transitions.[32] This does not rule out a "nucleation-and-growth" mechanism for this transformation. For identical reasons, the analogous transition between AlB_2- and $CaIn_2$-type structures is also not allowed by symmetry. An analogous molecular process is the bond-stretch isomerism in tricyclo[2.2.2.$0^{1,4}$]octane, **7**, which is a symmetry-forbidden

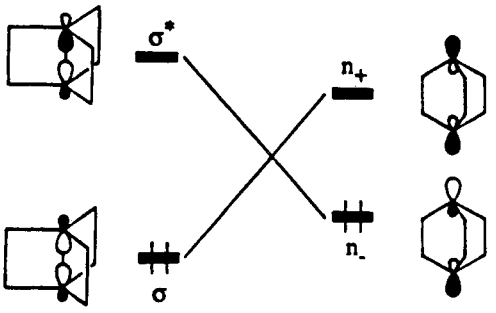

7

reaction as well. The generation of the bicyclic diradical from the propellane-type structure involves the crossing of the symmetric combination of lone-pair orbitals on positions 1 and 4 with the corresponding antisymmetric component.[33] High-pressure studies have yet to be performed on the solid-state compounds in order to determine whether such reactions may occur.[34]

In the previous discussion we have neglected the equatorial $p\sigma$ bands from influencing any of the geometrical changes in the stacking of 6^3 nets. Indeed, these orbitals interact between adjacent planes via π overlap, which at large separations is essentially zero and for smaller separations is significantly lower than the $p\sigma$ overlap between the π and π^* bands. Figure 8 illustrates how the Si–Si overlap populations both within and between each 6^3 net vary as a function of c/a. When these two distances are equal, the axial "bonds" (0.339) are still weaker than the equatorial bonds (0.637), and so distortions along the **c** axis will be preferred.

We have also mentioned possible transformations under elevated pressures in the AlB_2- and Ni_2In-type structures. In these systems, the large cations in the hexagonal prismatic holes will maintain a minimum separation between the 6^3 nets and prevent the π interactions of these $p\sigma$ bands from becoming significant. However, in wurtzite structures with no inserted cations, these overlap integrals may reach critical values under pressure. Under second-order Jahn–Teller arguments in the compressed Ni_2In framework, the coupling between the $p\sigma$ bands above and below the Fermi level may occur via an e_2 mode, which eventually leads to the NaCl-type structure. Figure 8 suggests that such a phonon mode will become increasingly effective. At elevated pressures, a number of compounds that occur with the wurtzite structure at 1 atm transform into the NaCl structure.[35] However, due to the difficulty of making accurate structure determinations at high pressure, the nature of this transition has not yet been investigated. Computations of a binary system with eight electrons per formula unit in wurtzite, rock salt, and N_2In-type geometries at constant volume rank the total energy per formula unit as E(wurtzite) < E(rock salt) (ΔE = +3.3 eV) < $E(Ni_2In)$ (ΔE = +4.1 eV). Thus, along an extremely specific reaction coordinate for the transformation of the wurtzite structure into the rock salt structure, a compressed Ni_2In structure without inserted cations represents a possible "transition state".

The $CaAl_2Si_2$ Structure and the $^2_\infty[Al_2Si_2]^{2-}$ Fragment

As we mentioned in the previous section, the $CaAl_2Si_2$ structure represents another example of eclipsed stacking of 6^3 nets. With these compounds we shall examine the third question raised concerning the effect of stoichiometry on the distortion coordinate of the primary AlB_2 network. Examination of the complete structure reveals that the distances between each alternant, puckered, honeycomb net in $CaAl_2Si_2$ alternate short–long–short–long. If we neglect the Ca atoms for the moment, we can begin with the Ni_2In framework and conclude from our previous arguments that distortion to the dimerized BN-type structure stabilizes this structure at four electrons per atom. If the hexagonal prismatic holes are either completely empty or completely occupied, the preferred distortion coordinate is the b_1 mode (at Γ, this mode transforms as a_{2u}), which leads to a wurtzite-type geometry.

The addition of cations in every other layer of hexagonal prismatic holes reduces the space group from $P6_3/mmc$ to $P\bar{3}m1$ and thereby facilitates the distortion toward a dimerized BN structure, which results from an a_1 (at Γ: a_{1g}) vibration. Second-order Jahn–Teller mixing between valence and conduction bands now requires that the modes transform as a_{1g}. The lower space group, moreover, does not limit each 6^3 net to remain planar. How can we understand the unusual local geometry at Si in $CaAl_2Si_2$?

Due to the two different atomic species in the covalent framework, we shall appeal to electrostatic interactions within the solid as a first approximation. In the case of $CaAl_2Si_2$, all scales of electronegativity (χ) rank the substituents according to increasing χ as χ(Ca) < χ(Al) < χ(Si). Therefore, Si should accumulate a net negative charge, while Ca will certainly be a cation (essentially a dication). The most primitive formalism assigns the compound as $Ca^{2+}(Al^{3+})_2(Si^{4-})_2$. Within the Zintl–Klemm rules the ionic formalism rationalizes much of the structural characteristics: (1) the $^2_\infty[Al_2Si_2]^{2-}$ network has four electrons per atom, in accordance with the coordination number of each Al and Si; (2) no direct Al–Al or Si–Si linkages occur. Yet the real picture cannot have such a

(32) Burdett, J. K.; Price, S. L. *Phys. Rev. B* **1982**, *25*, 5778.
(33) Stohrer, W.-D.; Hoffmann, R. *J. Am. Soc.* **1972**, *94*, 779.
(34) Kertesz, M.; Hoffmann, R. *J. Solid State Chem.* **1984**, *54*, 313.
(35) (a) O'Keeffe, M.; Hyde, B. G. *Acta Crystallogr., Sect. B* **1978**, *34*, 3519. (b) Bates, C. H.; White, W. B.; Roy, R. *Science* **1962**, 993. (c) Hazen, R. M.; Finger, L. W. *J. Appl. Phys.* **1986**, *59*, 3728.

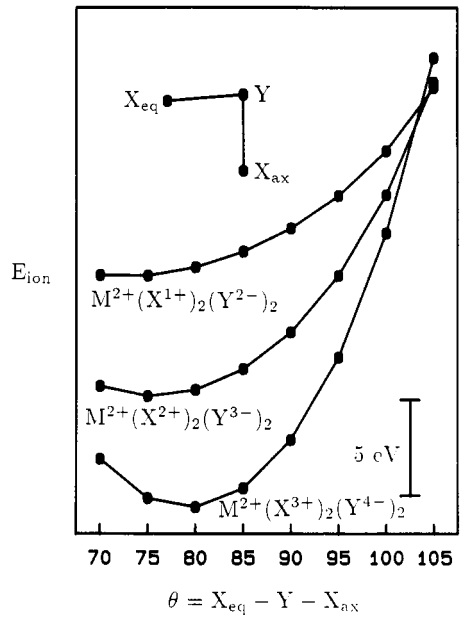

Figure 9. Total Madelung energy per unit cell as a function of the angle at the Si position for the $CaAl_2Si_2$ structure in three ionic formulations: (top) $M^{2+}X^{+}_2Y^{2-}_2$; (middle) $M^{2+}X^{2+}_2Y^{3-}_2$; (bottom) $M^{2+}X^{3+}_2Y^{4-}_2$. The absolute energy scale is arbitrary, but a 5-eV energy scale is indicated.

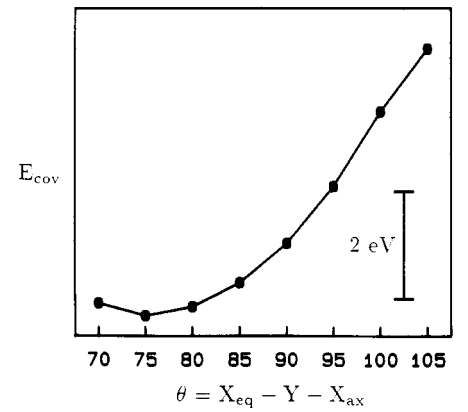

Figure 10. Total electronic energy as a function of the angle at the Si position in $CaAl_2Si_2$. A 2-eV energy scale is noted.

great disparity in the electron density at Al and Si. Figure 9 shows the total Madelung energy per unit cell plotted as a function of the Al_{ax}–Si–Al_{eq} angle, θ, for three charge distributions: (1) $M^{2+}(X^{+})_2(Y^{2-})_2$; (2) $M^{2+}(X^{2+})_2(Y^{3-})_2$; (3) $M^{2+}(X^{3+})_2(Y^{4-})_2$. All calculations were performed for equal unit cell volumes. In each case, the repulsions between the two different cations as well as the attraction between the M sites and the anions pucker the layers to give asymmetric coordination at the anion. Repulsions between the anions and between the cations within each sheet, moreover, give rise to the ionic energy minima that occur between 70 and 80°. This repulsive effect is clear given that the angle θ, which minimizes the Madelung energy, decreases as the absolute charge difference between X and Y decreases. The experimental angle in $CaAl_2Si_2$ (73.3°) is most closely predicted for case (1).

Can we understand the proper distortion from our band calculations? Figure 10 plots the total energy per unit cell as a function of θ, again by maintaining constant volume throughout the distortion. The minimum energy configuration is calculated at ~76° (the experimental angle is 73.3°). A comparison of the overlap populations between $CaAl_2Si_2$ in which one structure contains planar 6^3 AlSi nets and the other contains puckered 6^3 nets provides

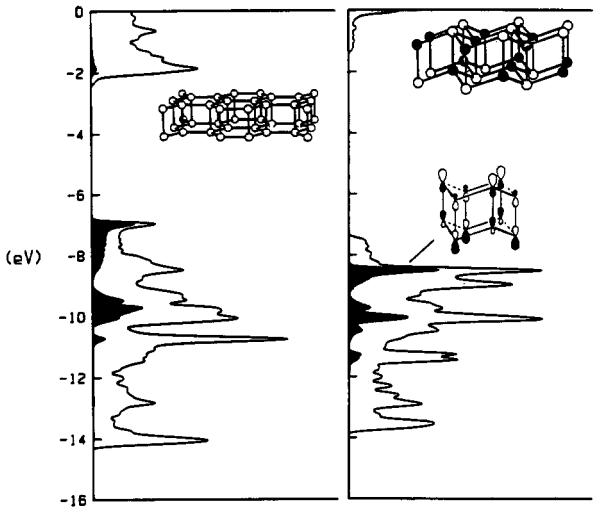

Figure 11. Projections of the σ-bonding combination of the intraplane π^* levels from the total DOS for the dimerized BN structure and the observed $CaAl_2Si_2$ frame. The cations were omitted from this calculations.

another rationale for the observed La_2O_3-type structure. As shown in 8, both the Si–Si and Al–Al interactions are

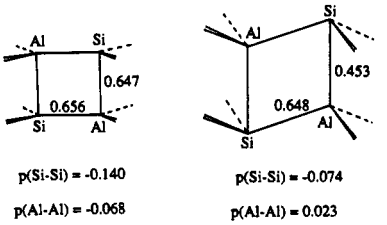

8

repulsive when each 6^3 net is planar with $|p_{Si-Si}| > |p_{Al-Al}|$. In concert with this, we find attractive Ca–Si and Ca–Al interactions, albeit weak, with $|p_{Ca-Si}| > |p_{Ca-Al}|$ (0.088 vs 0.040). Thus, we have two forces that act in parallel to produce the structure of $CaAl_2Si_2$ from the "partially intercalated" BN network: (1) the greater electrostatic or two-center four-electron repulsion between the more electronegative Si atoms; (2) the electrostatic attraction as well as the more favorable orbital overlap between Ca and Si. In addition, the overlap populations for the two symmetry-inequivalent Al–Si bonds (calculated for equal distances) correctly predict the relationship between these distances: $d_{ax} > d_{eq}$ ($p_{ax} < p_{eq}$). As the layers distort, the equatorial π^* interaction is weakened as σ_p overlap increases. Likewise, the s–p hybridization decreases the σ_p overlap in the axial bonds as it produces "lone-pair" orbitals on the Si atoms, 9. These two effects are shown in

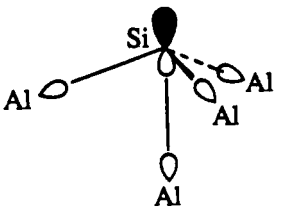

9

the DOS projections of Figure 11, which illustrate the σ-bonding combination of intraplane π^* orbitals for both the dimerized BN structure and the true $CaAl_2Si_2$ network. The stabilization of the observed structure with respect to the "idealized" geometry is immediately seen from the larger bandgap that results primarily from a decrease in the energy of the top of the valence band.

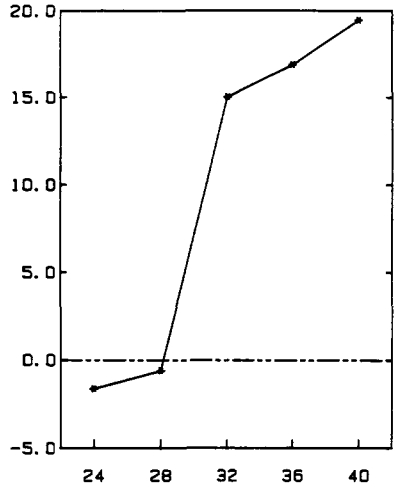

Figure 12. Energy difference curve as a function of electron number between the $BaAl_4$ and $CaAl_2Si_2$ modifications using Al and Si parameters. The coloring of the $BaAl_4$ net is as in $ThCr_2Si_2$ with Al in the Cr positions. When the energy difference is positive, the $CaAl_2Si_2$ structure is favored.

In accordance with expectations, the DOS diagram for the two-dimensional fragment $^2_\infty[Al_2Si_2]^{2-}$ differs little from the DOS for the complete three-dimensional structure – the interactions between adjacent bilayers are relatively weak. Therefore, when we consider these slabs as fundamental building units for other structure types, the crystal orbital of primary interest is the "lone pair" orbital on the more electronegative center, **10**, which occurs near the top of the valence band in the two-dimensional projection. In a later section, we shall examine certain structural possibilities when this orbital is incompletely occupied.

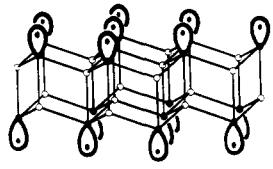

10

$BaAl_4$ vs $CaAl_2Si_2$

Among main-group systems, a structural isomer to the $CaAl_2Si_2$ system is the $BaAl_4$ prototype, **11**, which occurs

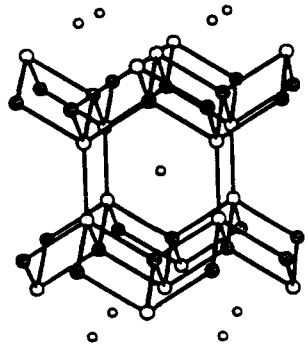

11

for numerous compounds.[5,36] Recently, Zheng and Hoffmann have discussed the electronic structure of $BaAl_4$ in sufficient depth that we shall not repeat the details.[13] As they have pointed out, the tetragonal $^2_\infty$[PbO]-layers, which stack along the **c** axis, may be conceptually derived from fcc Al. In general, the $BaAl_4$ structure is observed

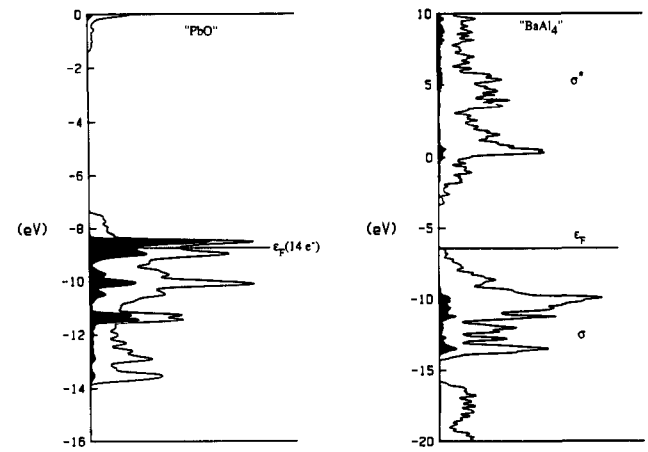

Figure 13. Total DOS for an isolated tetragonal $^2_\infty[Al_2Si_2]$ layer and combined to give the $BaAl_4$-type network. The projections of the p_z orbitals on the apex Si atoms are indicated in both diagrams.

for 14-electron systems, whereas $CaAl_2Si_2$-type compounds are mostly closed-shell 16-electron compounds.[5,37] A Mulliken population analysis on the aluminum network in $BaAl_4$ reveals that a smaller net charge accumulates on the tetrahedral sites ($q_{tet} = -0.15$) than on the five-coordinate apical sites ($q_{apical} = -0.85$). Therefore, in ternary systems we expect the most electronegative species to occupy the apical sites. For most examples, this is observed. However, the $^3_\infty[Be_2Ge_2]^{2-}$ net in $CaBe_2Ge_2$ is completely alternant such that in one tetragonal layer, the more electronegative Ge atoms occupy apical sites, and in the adjacent layer they occupy tetrahedral sites.[10] For the following discussion we limit our attention only to the charge distribution that occurs for the majority of cases as predicted by the Mulliken analysis. Extended Hückel calculations on each main-group framework using Al and Si atoms produce the energy difference curve shown in Figure 12 and correctly reproduce the experimental observations, even for the less common electron concentrations, e.g., the $BaAl_4$-type structure for $ThZn_4$.[5]

Again, we can use the method of moments to understand the results of the energy difference analysis.[31,38] Let us simply consider the two fragments from which each structure is constructed (**1** and **2**). Since each layer is an alternant structure, i.e., every atom is surrounded only by atoms of the other kind, we can safely count loops without including effects due to the different atomic species. In the tetragonal fragment, there are four four-rings per unit cell, while in the trigonal layer, there occur three four-rings and two six-rings. Since the difference first occurs with the number of four-rings, the energy difference curve will reflect a fourth moment, μ_4, disparity in the two systems. With $CaAl_2Si_2$ having the smaller μ_4 (fewer number of four-rings) as well as the larger μ_6 (greater number of six-rings), it is preferred for the half-filled band, while $BaAl_4$ types are electronically favored at counts both slightly less and greater than the half-filled point (four electrons per atom in the framework). Thus, for the most part, electronic influences on structural topology control these different observed geometries. We discuss this problem in a more global fashion elsewhere.[39] In addition, note that this analysis correctly predicts the structures of PbO and SnO (five electrons per atom) but not for Ba-

(36) Pearson, W. B. *J. Solid State Chem.* **1985**, *56*, 278.

(37) Nesper, R.; von Schnering, H. G.; Curda, J. *Z. Naturforsch., Teil B* **1982**, *37*, 1514.

(38) Burdett, J. K.; Miller, G. J. *J. Am. Chem. Soc.* **1987**, *109*, 4081.

(39) Burdett, J. K.; Canadell, E. *J. Am. Chem. Soc.*, to be submitted for publication.

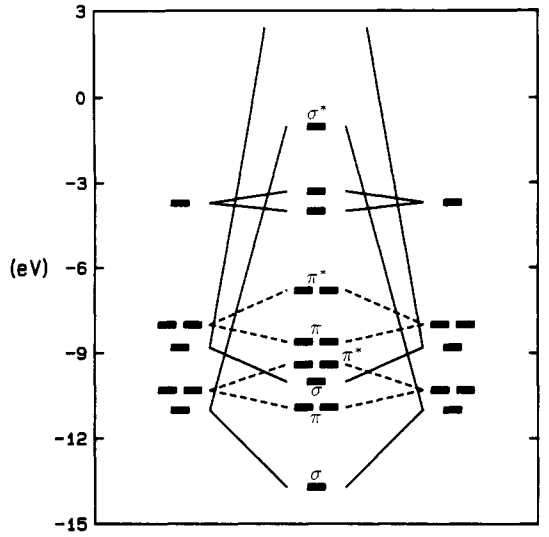

Figure 14. Interaction diagram at Γ between the two tetragonal fragments to form the $BaAl_4$ structure. σ and π interactions are indicated. The s orbitals on the more electronegative component lie below −15 eV.

Zn_2P_2 ($BaAl_4$ type),[40] BaMgSn (BiOCl type),[41] or InBi (PbO type).[22]

Using more traditional molecular orbital treatments, we can readily understand the energetic preference of $BaAl_4$ for counts less than the half-filled band. Figure 13 illustrates the projection from the total DOS of the p_z orbitals of the apical atom for the tetragonal $^2_\infty$[AlSi] layer, as well as the σ and σ^* combinations of these crystal orbitals in the condensed $BaAl_4$ system. For the isolated layer, band occupation up to 14 electrons per unit cell leaves the axial orbitals in the valence band partially occupied (16 electrons per unit cell would maximize Al–Si bonding in this layer and occupy all bands up to the energy gap). As in the $CaAl_2Si_2$ structure, the top of the valence band consists of two pairs of three fragment orbitals: two axial sp_z hybrid bands and four (p_x, p_y) bands, each of which is primarily centered on the more electronegative apical sites. These two sets of three orbitals for the individual layers represent the in-phase and out-of-phase combinations of mostly Si-centered p orbitals. As these sheets are brought together to give short, direct apical–apical linkages, the crystal orbitals at Γ interact according to the diagram in Figure 14. Since there are two slabs per unit cell, their crystal orbitals interact as in a simple dimer to give bonding (stabilized) and antibonding (destabilized) combinations. The (p_x, p_y) sets form π and π^* levels, whereas the axial sp_z hybrids form σ and σ^* orbitals between the layers (see also Figure 13). Since both σ^* combinations of the sp_z hybrids are significantly destabilized as opposed to the π^* orbitals in $BaAl_4$, 14 electrons per formula unit (two less than the half-filled point; 3.5 electrons per atom in the network) fill all σ-bonding orbitals, as well as the valence band interlayer π and π^* orbitals. We can visualize the fragments as in **12**, with each apical atom having one

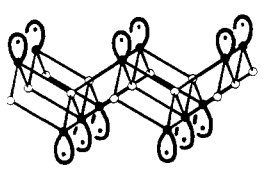

12

(40) Klüfers, P.; Mewis, A. *Z. Naturforsch., Teil B* **1986**, *33*, 151.
(41) Eisenmann, B.; Schäfer, H.; Weiss, A. *Z. Naturforsch., Teil B* **1970**, *25*, 651.

Table II. Geometrical Parameters of Selected $BaAl_4$ Structures[5]

struct	no. of e⁻	$d_{apex-apex}$, Å	$d_{apex-tet}$, Å
$CaCu_2Si_2$	12	2.308	2.425
$CaCu_2Ge_2$	12	2.476	2.455
$CaZn_2Al_2$	12	2.505	2.652
$SrCu_2Si_2$	12	2.420	2.465
$SrCu_2Ge_2$	12	2.462	2.517
$ThZn_4$	12	2.486	2.526
$NaGa_4$	13	2.663	2.570
KIn_4	13	3.076	2.921
$RbIn_4$	13	3.128	2.955
$SrCu_{1.75}P_2$	13.75	2.296	2.431
$CaAl_4$	14	2.662	2.614
$CaGa_4$	14	2.577	2.581
$SrAl_4$	14	2.652	2.648
$SrGa_4$	14	2.611	2.607
$BaAl_4$	14	2.664	2.686
$BaGa_4$	14	2.659	2.661
$BaIn_4$	14	2.808	2.923
$CaZn_2Ge_2$	14	2.474	2.571
$CaCu_2P_2$	14	2.251	2.381
$BaZn_2P_2$	16	3.685	2.486

half-filled sp_z hybrid orbital ready to σ overlap with a neighboring layer. In this sense, the bonds between each $^2_\infty[Al_2Al_2]^{2-}$ layer are two-center two-electron bonds with the remaining 12 electrons per slab delocalized in multicenter bonding within each layer.

For the electron-deficient 12-electron systems, such as $ThZn_4$, $CaAl_2Zn_2$, and $SrCu_2Ge_2$,[5] the highest π^* orbital in the valence band will be depleted and lead to stronger and, perhaps, shorter apical–apical bonds. Table II lists a number of 12-, 14-, and 16-electron $BaAl_4$-type systems along with the two symmetry-inequivalent distances in the covalent framework (by no means is this list exhaustive!). Although our expectations concerning the 12-electron materials are confirmed by these examples, we note that two potentially important contributions to the electronic structure of these compounds have been omitted: (1) interactions with the additional cations; (2) inclusion of lower lying d orbitals, especially for Cu and Zn systems.

If we proceed to higher electron counts, e.g., the 16-electron compound, $BaZn_2P_2$, what are the structural consequences of these extra electrons on compounds of this type? Given our simple picture in **12**, two additional electrons will complete the occupation of the frontier sp_z hybrid orbitals. Any subsequent interaction between these layers will be destabilizing due to a two-center four-electron repulsion (as in He_2). In $BaZn_2P_2$, electrostatic attraction between Ba^{2+} and the tetragonal $^2_\infty[Zn_2P_2]^{2-}$ provides the $BaAl_4$-type network (i.e., it controls the relative arrangement of adjacent tetragonal layers), while the closed-shell repulsions maintain long P–P separations (3.675 Å, $(P\cdots P)^{6-}$) rather than typical P–P "single bond" distances (2.2–2.3 Å, $(P-P)^{4-}$). In compounds isotypic with BaMgSi,[5] the $^2_\infty[Mg_2Si_2]^{2-}$ layers are interspersed with two sheets of cations such that no direct linkages occur between these fragments as well.

Beyond the half-filled point (>16 electrons per layer), electrons must occupy states that are X–Y antibonding within each sheet and, therefore, may disrupt their tetragonal symmetry. One such example concerns the conceptual bond-breaking process in the $BaAl_4$ structure to form the orthorhombic series $M_3Al_2Si_2$ (M = alkaline-earth metal). We illustrate the transformation of the main-group network (minus the cation species) in **13**. The standard description of $M_3Al_2Ge_2$ materials is as an ordered variant of the Ta_3B_4 structure, in which we find polyacene-type chains of formula $^1_\infty[Al_2Ge_2]^{6-}$.[42] This represents a Zintl

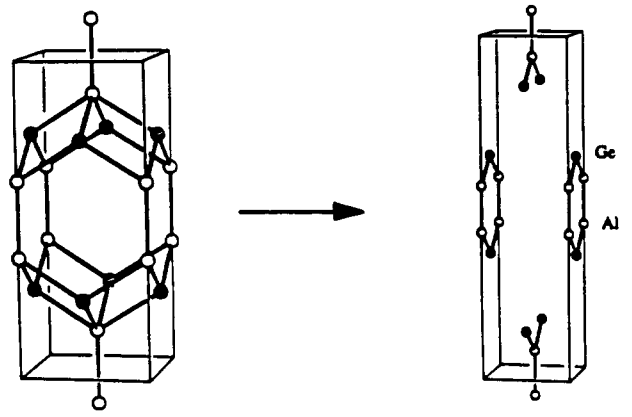

13

compound, since planar three-coordinate Al is assigned Al^- (isoelectronic with Si) and two-coordinate Ge is assigned Ge^{2-} (isoelectronic with Se) to give $(Al^-)_2(Ge^{2-})_2$. Note that the more electronegative element occupies the site with lower coordination number. We can again invoke the moments method[43] to understand the site preference problem. With respect to only the four π bands in a polyacene chain,[25] binary AB systems adopt a completely alternant arrangement of A and B atoms from fourth moment differences,[31] when the π system is half-occupied. In $^1_\infty[Al_2Ge_2]^{6-}$, the π-system is three-fourths occupied, i.e., six electrons are in the π system, and thereby produces Al–Al contacts.

For the hypothetical transformation in **13**, the square nets of atoms at $z = 0.25$ and 0.75 in $BaAl_4$ are severely distorted (these are the tetrahedral sites in the Al net). Furthermore, the more electronegative atoms now occupy these positions rather than the "apical" sites, while the apical–apical bonds remain intact. Although not shown in **13**, one cation site in $M_3Al_2Ge_2$ is the same as in $BaAl_4$, while two additional cations insert themselves between the "disrupted layers."

For electron counts above the half-filled point, the tetragonal layer need not be "destroyed" if the X–Y orbitals interactions are sufficiently weak in this energy regime. A Mulliken population analysis on a monatomic $^2_\infty$[PbO]-type network reveals that the charge characteristics of the two sites are reversed from the charge preference for counts less than the half-filled case, i.e., the electronegative constituent occupies the tetrahedral sites. These results are confirmed by SnO, PbO, and BiOCl,[7] which may be formulated $[BiO]^+Cl^-$. Since the cations in these compounds have energetically low-lying, as well as contracted, s orbitals, the two additional electrons per formula unit are assigned to these inert pair orbitals. Thus, such layers are isolobal to the 16-electron sheets, e.g., $^2_\infty[Mg_2Sn_2]^{4-}$, and we expect no short, direct apical–apical bonds, i.e., no Pb–Pb or Sn–Sn bonds between adjacent sheets. With two fewer electrons the layer is now isolobal to the 14-electron fragments. Will short metal–metal bonds forms? We need to consider such layers as $^2_\infty[PbO]^+$ or $^2_\infty[BiO]^{2+}$, which means formally Pb(III) or Bi(IV) cations. However, the structural chemistry of Pb and Bi compounds indicates the thermodynamic stability of Pb(II)/Pb(IV) and Bi(III)/Bi(V) rather than the intermediate oxidation states.[7] One series of 18-electron sheets occurs in $MBiO_2X$ (M = Ba or Cd; X = halide),[44] which are formulated as $[MBiO_2]^+X^-$. With the M and Bi atoms randomly distributed through the apical sites, these compounds are isotypic to $ThCr_2Si_2$. There occur formally M(II) and Bi(III) with metal–metal separations of ca. 4.0 Å, which suggest stronger electrostatic repulsions than any sort of donor–acceptor interaction between the cations.

Building Solids by Using the Trigonal $^2_\infty[Al_2Si_2]$ and Tetragonal $^2_\infty$[PbO] Layers

The $BaAl_4$ structure results primarily because the σ bonding between the fundamental $^2_\infty$[PbO]-type fragments with 14 electrons is maximized (Figure 13). An examination of the DOS for the $^2_\infty[Al_2Si_2]^{2-}$ slab of $CaAl_2Si_2$, but this time for 14 electrons, reveals as well the possibility of direct linkages with adjacent slabs occurring at the apical sites (**10**). A recently reported Cu–Fe–S mineral, nukundamite ($Cu_{3.61}Fe_{0.39}S_2$), contains this structural motif providing direct S–S linkages.[45] In main-group systems, direct connection of these puckered bilayers has yet to be observed, but there do exist structures that involve the trigonal $^2_\infty[Al_2Si_2]$ slab in direct σ interactions with other fragment types.

One example is Al_4C_3 and the entire series of aluminum carbonitrides, $Al_xC_yN_z$, shown in Figure 15.[46] This series of structures contains three characteristic fragments: (1) the puckered bilayers, $^2_\infty[Al_2C_2]$; (2) anti-CdI_2-type layers, $^2_\infty[Al_2C]$; (3) puckered 6^3 sheets, $^2_\infty$[AlN]. These compounds may then be described by using these components as $[Al_2C_2]_{(-x+2y+z)/2}[Al_2C]_{(x-y-z)}[AlN]_z$. In the pure carbide ($z = 0$), slabs of type (1) alternate with the anti-CdI_2 sheets. Such isolated layers have been reported for Cs_2O and the alkaline-earth metal nitrides, Ca_2N and Ba_2N,[47] although more recent work suggests these nitrides to be stabilized by hydrogen.[48] In Al_4C_3 simple electron counting assigns 14 electrons to the $^2_\infty[Al_2C_2]$ slab and 10 electrons to the $^2_\infty[Al_2C]$ layer. The basic interactions between these fragments that stabilize the structure are the two σ-bonding interactions involving the axial orbitals of the apical atoms for each fragment. We are already familiar with the situation for the $^2_\infty[Al_2C_2]$ slab, but what occurs in $^2_\infty[Al_2C]$? With 10 electrons, the four C orbitals are completely occupied to provide Al–C bonding. The extra two electrons begin to fill the conduction band, which has exclusively Al character. The lowest lying level in the conduction band occurs at M in the two-dimensional hexagonal Brillouin zone as it contains no C s or p component, **14**. Locally, at the octahedral C atom, these levels

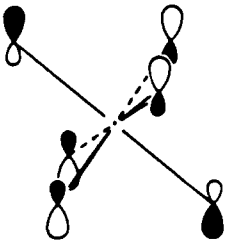

14

are derived from the e_g orbital in an "Al_6C" octahedron, which is not an appropriate representation for the C 2s (a_{1g}) or the 2p (t_{1u}) orbitals. Since the Fermi level for neutral

(42) (a) Widera, A.; Eisenmann, B.; Schäfer, H.; Turban, K. *Z. Naturforsch. Teil B* **1976**, *31*, 1592. (b) Widera, A.; Schäfer, H. *Ibid.* **1977**, *32*, 1349.
(43) Burdett, J. K. *Struct. Bonding* **1987**, *65*, 30.
(44) (a) Sillén, L. G. *Z. Anorg. Allg. Chem.* **1941**, *246*, 331. (b) Sillén, L. G.; Gjörling-Husberg, A. S. *Ibid.* **1941**, *248*, 135.
(45) Sugaki, A.; Shima, H.; Kitakaze, A.; Mizota, T. *Am. Mineral.* **1981**, *66*, 398.
(46) Jeffrey, G. A.; Wu, V. Y. *Acta Crystallogr.* **1963**, *16*, 559.
(47) Keve, E. T.; Skapski, A. C. *Inorg. Chem.* **1968**, *7*, 1757.
(48) Brice, J.-F.; Motte, J.-P.; Aubry, J. *Rev. Chim. Miner.* **1975**, *12*, 105.

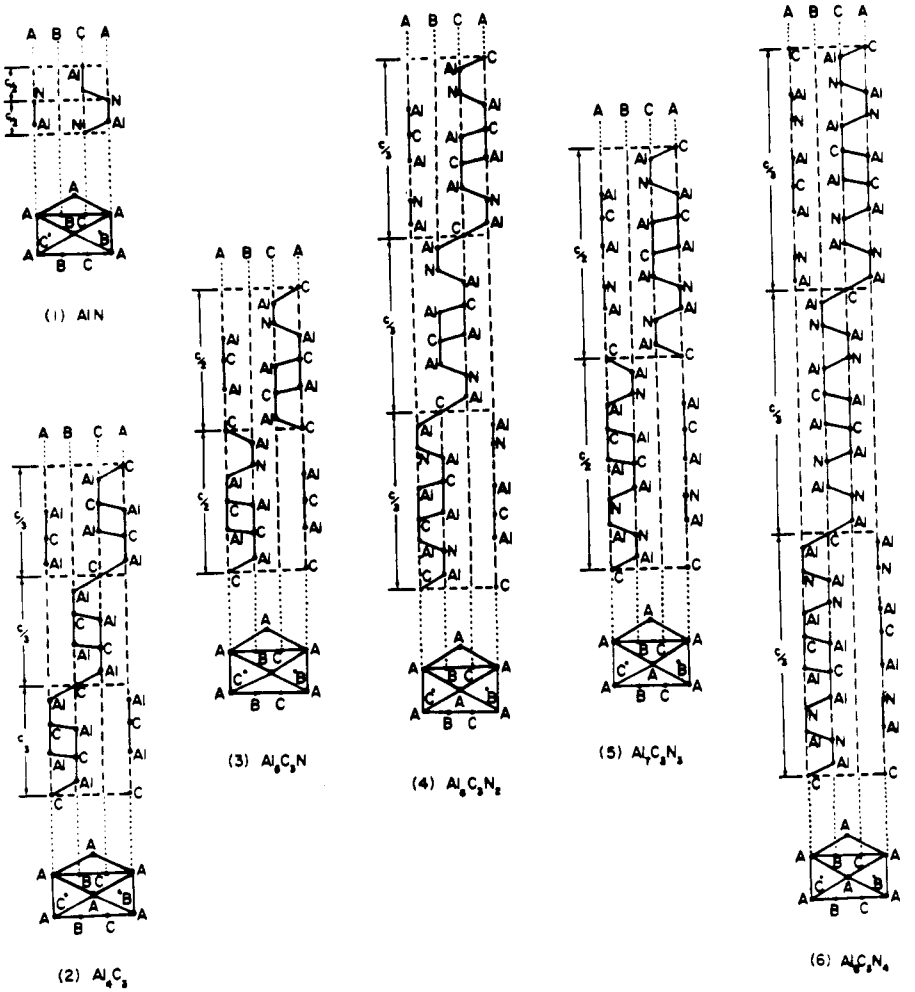

Figure 15. Schematic structures of AlN, Al_4C_3, and a variety of the aluminum carbonitrides, $Al_xC_yN_z$ (taken from ref 46).

$^2_\infty[Al_2C_2]$ lies within the C manifold, whereas the Fermi level for $^2_\infty[Al_2C]$ is in the Al region, we may consider Al_4C_3 in the donor–acceptor formulation, $[Al_2C]^{2+}[Al_2C_2]^{2-}$, to produce a closed-shell insulator. The total DOS for Al_4C_3 as well as for the separate fragments is shown in Figure 16. Comparison of these three DOS diagrams indicates that the σ interactions between the frontier orbitals on the two fragments are important in generating the large gap between valence and conduction bands in Al_4C_3. Note how the Al-centered orbitals at the bottom of the conduction band of the $^2_\infty[Al_2C]$ layer are destabilized by this σ overlap. If the interactions between these fragments were relatively weak and involved only formal charge transfer, we would then observe narrow-gap semiconducting properties in this compound (E_F for $[Al_2C]^{2+}$ occurs at the narrow minimum in the DOS slightly above −10.0 eV).

The carbonitride structures contain puckered 6^3 sheets of AlN inserted between two carbide fragments. These insertion products further confirm the donor–acceptor nature of the Al_2C and Al_2C_2 fragments, respectively, as well as the importance of the σ overlap between the frontier orbitals toward stabilizing these compounds. Each N atom (with two electrons in its lone pair sp hybrid orbital) is always in close contact with the Al of $^2_\infty[Al_2C]$, while the apical C atom in the $^2_\infty[Al_2C_2]$ slab bonds with the Al site (with an empty acceptor $3p_z$ orbital) in the AlN sheet. Again, the orbital interactions significantly affect the bottom of the conduction band in the $^2_\infty[Al_2C]$ fragment.

The structure of CaLiSn[49] (actually $CaLi_{0.95}Sn_{1.05}$) is

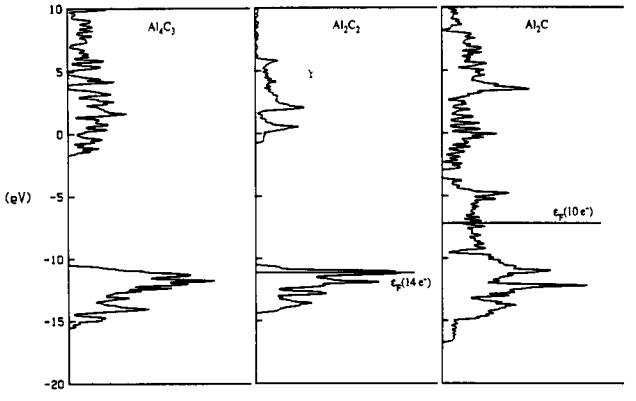

Figure 16. Total DOS for (left) Al_4C_3, (middle) the $^2_\infty[Al_2C_2]$ fragment, and (right) the $^2_\infty[Al_2C]$ fragment.

similar to the carbonitrides of aluminum except that they contain no CdI_2-type layers: $^2_\infty[Li_2Sn_2]^{x-}$ slabs alternate with puckered 6^3 nets $^2_\infty[LiSn]^{y-}$. By necessity, there are now both Li–Sn and Sn–Sn axial bonds between the two fragments since Sn atoms occupy apical sites in the $^2_\infty[Li_2Sn_2]$ slabs. Direct contacts between the two fragments as well as the occurrence of Sn–Sn bonds result from each having fewer than four electrons per component, which would introduce holes in the anion band for a completely alternant framework.

Both 14- and 16-electron $^2_\infty[PbO]$-type layers may also be combined with other two-dimensional fragments to form new solids. For example, the $BaCuSn_2$ structure contains layers of parallel polyacetylene-type chains $^1_\infty[Sn_2]$

(49) Müller, W.; Voltz, R. *Z. Naturforsch., Teil B* **1974**, *29*, 163.

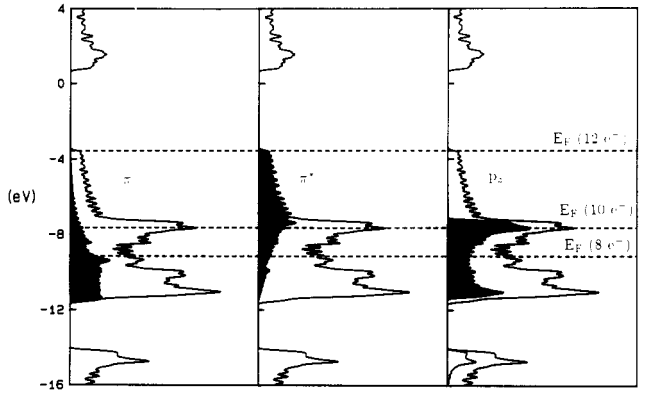

Figure 17. DOS projections for a single $^2_\infty$[BaSn] slab extracted from the CrB-type structure: (left) π band along the chain; (middle) π^* band along the chain; (right) p_z band that points toward the empty vertex for planar three-coordination of the Sn atoms. The dashed lines indicate Fermi levels for four, five, and six electrons per Sn atom.

alternating along the c axis with $^2_\infty$[Sn_2Cu_2] tetragonal sheets, **15**.[11,50] Given the arrangement of cations sur-

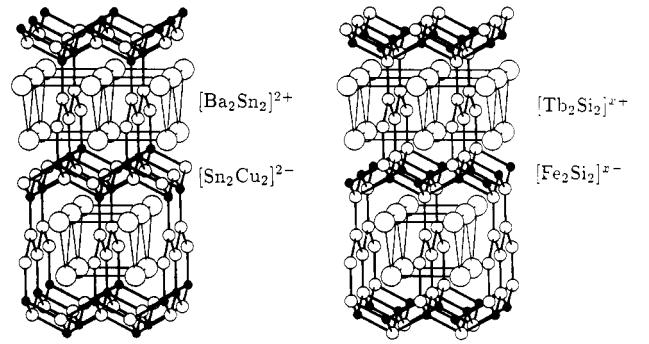

15

rounding the zigzag chains, we recognize each $^2_\infty$[Ba_2Sn_2] slab as a fundamental layer from the CrB-type structure of BaSn, which occurs for several alkaline-earth metal and lanthanide monotetralides.[51] (Note: Parthé and Chabot describe the $BaCuSn_2$ structure as an intergrowth of $BaAl_4$- and AlB_2-type slabs[52]).

Figure 17 illustrates various projections from the DOS of the $^2_\infty$[Ba_2Sn_2] fragment. Although we consider this as a layer, the one-dimensional nature of the interactions are clearly evident from the Sn $5p_z$ component given the shape of its projection. However, partial orbital overlap between adjacent chains produces incomplete separation of the π and π^* bands along each chain. The appearance of the Sn $5p_z$ band in this frontier region is particularly noteworthy. Since this orbital points toward the vacant capping site in the tricapped trigonal prismatic coordination sphere of each Sn atom (six by Ba and only two by Sn; refer to the left side of **15**), it remains a frontier orbital that is well suited to interact with an appropriate σ-type orbital from other fragments. In the $^3_\infty$[$CuSn_2$]$^{2-}$ network these are the tetragonal $^2_\infty$[Cu_2Sn_2] layers, whose DOS and certain important projections are shown in Figure 18.

When these two pieces are brought together to form the complete $BaCuSn_2$ network, how do they attain electronic equilibrium? Given the various Fermi levels indicated in

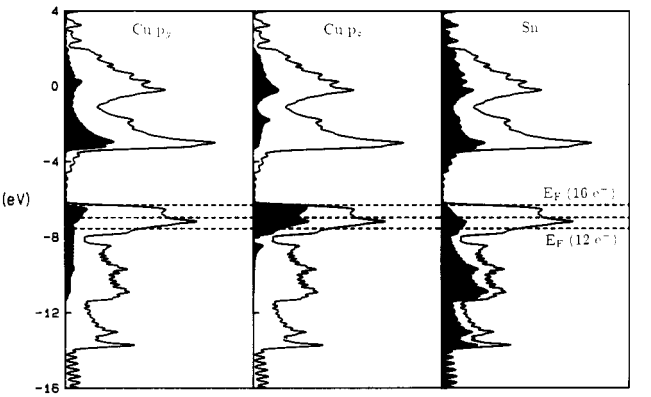

Figure 18. DOS projections for a single $^2_\infty$[Sn_2Cu_2] tetragonal layer: (left) Cu p_y band that will interact with the π and π^* bands in the CrB fragment; (middle) Cu p_z band that forms σ and σ^* orbitals with the chain; (right) the total Sn contribution in the 4^4 nets. The dashed lines indicate Fermi levels for 12, 14, and 16 electrons per layer.

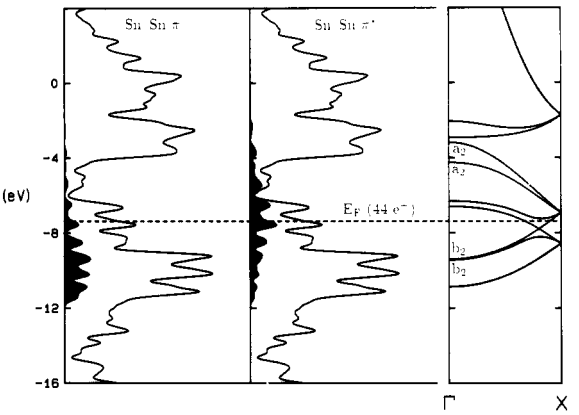

Figure 19. π and π^* projections from the $^1_\infty$[Sn_2] chains in $BaCuSn_2$. The dashed line indicates the Fermi level for 44 electrons per unit cell. On the right, we illustrate the π energy band scheme. As there are two chains per unit cell, the two π and π^* bands are correspondingly labeled. Interactions between the chains account for populating some of the π^* band.

each fragment DOS in Figures 17 and 18, the neutral $^2_\infty$[Ba_2Sn_2] slab will donate electrons to the tetragonal layer. If the two fragments do not interact, then they will at least match Fermi levels, i.e., chemical potentials, to give the calculated ionic formulation $[Ba_2Sn_2]^{2+}[Sn_2Cu_2]^{2-}$. However, from **15** we clearly see the direct contacts between the two slabs. The total DOS of the complete three-dimensional network (see Figure 19) shows the effects of this particular geometry. Strong σ interactions between the Sn $5p_z$ and Cu $4p_z$ orbitals remove these components near the Fermi level by forming bonding and antibonding combinations. The Cu–Sn π interactions are substantially weaker since the position and the dispersion of the Sn–Sn π and π^* bands in $BaCuSn_2$ have changed little from those in the fragment, $^2_\infty$[Ba_2Sn_2]. The π manifold along ΓX in the orthorhombic Brillouin zone (parallel to the chain direction) suggests maximization of π conjugation along the $^1_\infty$[Sn_2] chain, although the DOS projections reveal some Sn–Sn π^* character below the Fermi level due to interchain orbital overlap. The COOP curves for intrachain Sn–Sn and interlayer Cu–Sn bonds indicate that the Cu–Sn interactions obtain their maximum overlap population for the electron count in $BaCuSn_2$ (Figure 20). If we refer back to Figure 13 concerning the bonding in $BaAl_4$, we conclude that these Cu–Sn interactions maximize their π overlap as well. Therefore, from this analysis, we assign 12 electrons to the $^2_\infty$[Cu_2Sn_2] layer and obtain the same ionic formula as above.

(50) Dörrscheidt, W.; Savelsberg, G.; Stöhr, J.; Schäfer, H. *J. Less Common Met.* **1982**, *83*, 269.
(51) (a) Schob, O.; Parthé E. *Acta Crystallogr.* **1965**, *19*, 214. (b) Hohnke, D.; Parthé, E. *Ibid.* **1966**, *20*, 572.
(52) Parthé, E.; Chabot, B. *Handbook on the Physics and Chemistry of Rare Earths*; Gschneider, K. A., Eyring, L., Eds.; Elsevier-North-Holland: Amsterdam, 1979; Vol. 2, pp 113–334.

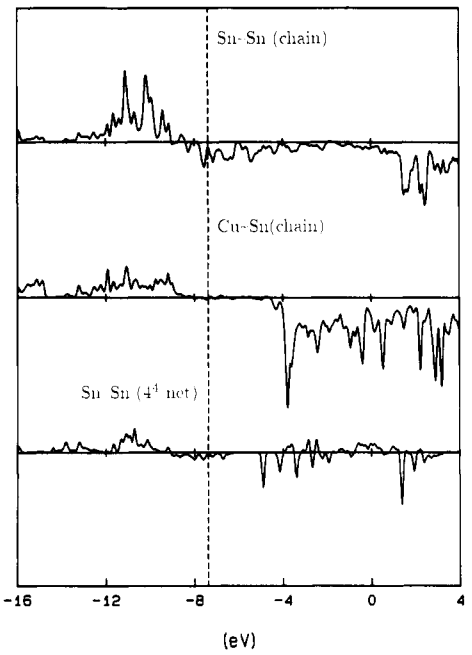

Figure 20. COOP curves for (top) Sn–Sn bonds within the chains; (middle) Cu–Sn bonds between the tetragonal layer and the CrB-type fragment; (bottom) Sn–Sn within the 4^4 net in the tetragonal layer. The Fermi level for $BaCuSn_2$ is shown by the dashed line.

We have necessarily avoided assigning formal charges to each of the atoms in the three-dimensional network due to the ambiguity in how to select the more electronegative atom between Cu and Sn. The Pauling scale ranks χ(Sn) (=1.93) slightly above χ(Cu) (=1.90). Previous arguments indicate that the apical sites of the $^2_\infty$[PbO] layer accumulate more charge for counts up to the half-filled band and thus represent the preferred sites for the more electronegative constituent. A calculation on the $^3_\infty[CuSn_2]^{2-}$ network of $BaCuSn_2$ using only a single atom type (Si) and equal nearest-neighbor distances (2.45 Å) reveals the same behavior as earlier computations except that the chain atoms accumulate even more charge than the apical sites (q(chain) = 4.15; q(apical) = 3.72; q(tet) = 3.13). Thus, given the relative electronegativities of Cu and Sn, the optimal coloring pattern should lead to $^1_\infty[Sn_2]$ chains, **16**,

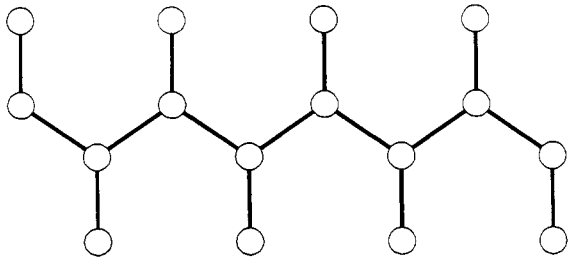

16, $\infty[Sn_2]$

that are interconnected via 4^4 nets of Cu atoms in the tetrahedral sites. Such isolated chains are found for $^1_\infty[B_2C_2]$ in UBC,[22] whose optimal electron count is 22 electrons. If we assign Cu as Cu(I), then $[Sn_2]^{3-}$ would maximize the electronic stability of **16**. This arrangement occurs for the Si atoms in $TbFeSi_2$, and Parthé and Chabot suggest that many of the rare-earth metal–transition metal tetralides reported to have the $BaCuSn_2$ structure actually adopt the configuration in $TbFeSi_2$.[51]

However, the chains that occur in $BaCuSn_2$ are of the type **17**. The stability of this atomic distribution in the $^3_\infty[CuSn_2]^{2-}$ net is related to the factors that control the

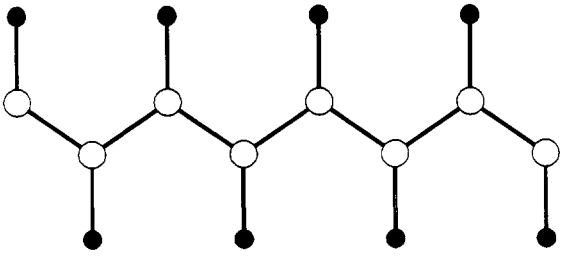

17, $\infty[CuSn]$

$CaBe_2Ge_2$ structure type, which, incidentally, occurs for $LaCu_2Sn_2$.[5] All known compounds have rather large differences in the relative sites of the constituents of the network and small differences in their electronegativities. As Zheng and Hoffmann point out,[17] the donor–acceptor interaction between the two kinds of tetragonal sheets becomes the more dominant force as the principal quantum number of the s and p orbitals on the more electronegative component increases. Their analysis suggests that $CaBe_2Ge_2$ may be formulated as $Ca^{2+}Be^{2+}{}_2Ge^{4-}Ge^{2-}$ ($=Ca^{2+}[BeGe]^{2-}[BeGe]^0$) rather than $Ca^{2+}Be^{2+}{}_2Ge^{3-}{}_2$ ($=Ca^{2+}[BeGe]_2^-$). The formally neutral tetragonal sheet implies Ge^{2-}, isoelectronic to Se, and suggests that some bonding interactions between Ge atoms in the 4^4 sheets remain. In $BaCuSn_2$ with Sn atoms in the tetrahedral sites, the overlap population in the 4^4 net indicates a significant bonding interaction (p_{Sn-Sn} = 0.30, Figure 20), whereas for the alternative coloring with Cu atoms in the these sites, essentially no Cu–Cu overlap occurs, and the interaction is even slightly repulsive (p_{Cu-Cu} = –0.02). Thus, configuration **17** occurs in $BaCuSn_2$ due to the increased stability of the inverse coloring of the tetragonal slab (with Sn in the tetrahedral sites) and the greater significance of the donor–acceptor interaction between the two fragments. In $TbFeSi_2$ and related compounds, much greater electronic stability occurs for the homonuclear chain **16** and the normal coloring of the tetragonal slab.

Other sets of examples that utilize the $^2_\infty$[PbO]-type tetragonal fragment include the $SrZnBi_2$ (*I*4/*mmm*) and $CaMnBi_2$ (*P*4/*mmm*) structure types, in which a square net of Bi atoms is inserted between two $^2_\infty[Zn_2Bi_2]$ or $^2_\infty[Mn_2Bi_2]$ tetragonal layers, **18**.[5] An orthorhombic dis-

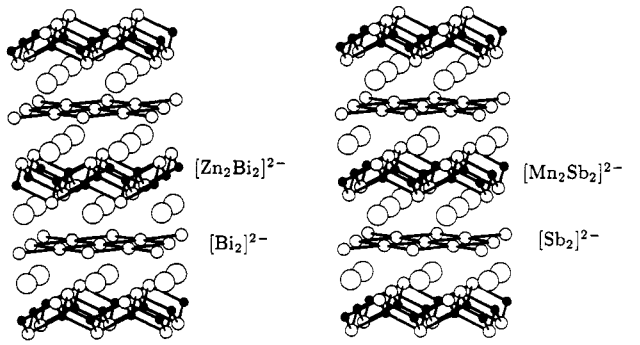

18

tortion of $CaMnBi_2$ occurs when Sb atoms occupy the Bi sites for certain combinations of cations, e.g., $CaMnSb_2$ and $SrMnSb_2$. Each square net is distorted to give zigzag $^1_\infty[Sb_2]$ chains. Since the topology in these structures is similar, we shall neglect their differences for our discussion (electronic influences on the orthorhombic distortion have been discussed by Tremel and Hoffmann[53]) and consider $SrZnBi_2$ as the prototype. There are no direct (apical Bi)–(square net Bi) linkages, and so we assign 16 electrons

(53) Tremel, W.; Hoffmann, R. *J. Am. Chem. Soc.* **1987**, *109*, 124.

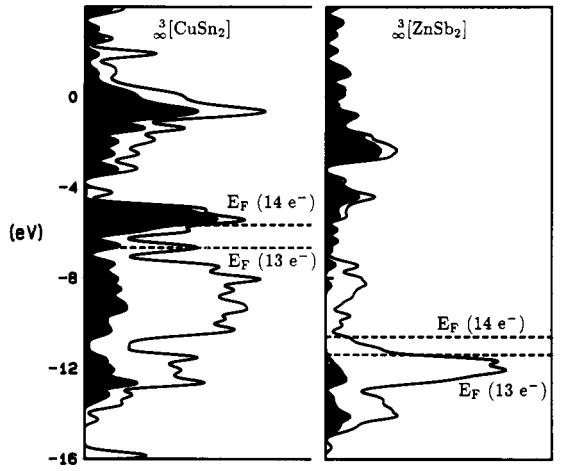

Figure 21. Comparison of the DOS for two different cases of the $BaZnBi_2$ structure: (left) small electronegativity difference between the atoms in the net, $[CuSn_2]$; (right) larger electronegativity difference as observed in $BaZnSb_2$. The shaded portion is the projection of the total orbital contribution from the atoms in the tetrahedral sites (Zn sites). Dashed lines point out Fermi levels for 13 and 14 electrons per formula unit.

to the PbO-type network: $^2_\infty[Zn_2Bi_2]^{2-}$. This results in setting the square net as Bi_2^{2-}, isoelectronic to Po, which adopts a simple cubic framework. We have used the moments method to understand the occurrence of four-rings in the α-Po structures.[31]

Two classes of compounds occur with the $BaZnBi_2$-type structure, and each has a characteristic electron concentration. The first includes these ternary phases we have already mentioned with 14 electrons per formula unit. The second class are AB_3 compounds in which A is a group 4 element (Ti, Zr, or Hf) and B is a group 13 element (Al, Ga, or In).[5] This collection of compounds has 13 electrons per formula unit. The most visible difference between these two classes is the relative electronegativities of atoms occupying the "covalent" network, i.e., $^3_\infty[ZnBi_2]^{2-}$ vs $^3_\infty[Al_3]$. Figure 21 illustrates the effect on the DOS for large and small electronegativity differences. When this disparity is small, the Fermi level for 14 electrons crosses states with significant contributions from atoms in the tetrahedral sites of the tetragonal fragment (1). These levels are strongly antibonding between both types of bonds within these fragments. One less electron per formula unit leads to maximum bonding within these layers, and the resulting formalism for $ZrAl_3$ as $[Al_2Al_2]^{4-}[Al_2]^{4-}$. Note that the square net of Al is isoelectronic to phosphorus, which under pressure transforms to a simple cubic modification.[54]

Other Systems

In this paper, we have considered only main-group systems that include the trigonal $^2_\infty[Al_2Si_2]^{2-}$ or tetragonal $^2_\infty$[PbO] layer as fundamental structural building units. We have seen how their valence electron concentrations control modes of connectivity to form a diverse collection of compounds. There exist numerous transition-metal compounds that utilize these fragments as well. For example, the tetragonal layers are found isolated in mackinawite (FeS)[55] and CaMnGe,[56] as well as connected to form the $ThCr_2Si_2$ structure types,[5] while the trigonal slabs occur isolated as in $CaMn_2P_2$[57] and connected as in nukundamite.[45] In all cases, the transition metal occupies the tetrahedral sites. An interesting sequence of telluride compounds finds the trigonal layers in NiTe[22] and PtTe[58] and the tetragonal slabs in CuTe[59] (NiTe has only been reported as a thin film), which suggests that an electronic effect governs these structures as well.

Table III. Atomic Parameters for Extended Hückel Calculations

atom	orbital	H_{ii}, eV	ζ
Si	3s	-17.30	1.63
	3p	-9.20	1.43
Al	3s	-12.30	1.37
	3p	-6.50	1.36
Ca	4s	-7.00	1.10
	4p	-4.00	1.10
C	2s	-21.40	1.63
	2p	-11.40	1.63
Cu	4s	-11.40	2.20
	4p	-6.06	2.20
Sn	5s	-17.30	2.13
	5p	-8.90	1.82
Zn	4s	-12.41	2.01
	4p	-6.53	1.70
Sb	5s	-18.80	2.32
	5p	-11.70	2.00

Acknowledgment. This research was supported by The National Science Foundation by NSF DMR 8414175.

Appendix

Many of the calculations described in this paper used the extended Hückel method within the framework of the tight-binding approximation.[20] The atomic parameters are listed in Table III. Integrated quantities, e.g., total energies, charges, and overlap populations, as well as DOS diagrams were determined by using special points sets[60] in the corresponding Brillouin zones. Madelung energies were calculated by using the Ewald method[61] and excluded all Born repulsion terms.

Specific relevant details concerning specific parts of this article are as follows:

$AlB_2 \rightarrow CaIn_2$: Si parameters; all short Si–Si distances set to 2.45 Å; 252 special points.

$Ni_2In \rightarrow$ LiGaGe: Al and Si parameters; all short Al–Si distances were 2.45 Å; 126 special points.

$CaAl_2Si_2$: Conditions similar to the $Ni_2In \rightarrow$ LiGaGe section were employed. The Al–Si distance of 2.45 Å corresponds to the weighted averaged Al–Si distance in $CaAl_2Si_2$.

$BaAl_4$: The reported geometry for $BaAl_4$ as well as a model $^3_\infty[Al_2Si_2]$ net were used; 125 k points in the tetragonal Brillouin zone.

Al_4C_3, et al.: Experimental geometries for all compounds in this class and 126 special k points in the three-dimensional hexagonal zone. DOS for each two-dimensional fragment were determined using 252 points in the two-dimensional zone.

$BaCuSn_2$ and $BaZnBi_2$: Again, reported structural parameters with 64 (orthorhombic) and 75 (tetragonal) special points.

(54) Kikegawa, T.; Iwasaki, H. *Acta Crystallogr., Sect. B* **1983**, *39*, 158.
(55) Bertaut, E. F.; Burlet, P.; Chappert, J. *Solid State Commun.* **1965**, *3*, 335.
(56) Dörrscheidt, W.; Schäfer, H. *Z. Naturforsch. Teil B* w1976, *31*, 1050.
(57) Mewis, A. *Z. Naturforsch. Teil B* **1978**, *33*, 606.
(58) Bhan, S.; Gödecke, T.; Schubert, K. *J. Less Common Met.* **1969**, *19*, 121.
(59) Hulliger, F. *Struct. Bonding* **1968**, *4*, 83.
(60) Chadi, D. J.; Cohen, M. L. *Phys. Rev. B* **1973**, *8*, 5747.
(61) Ziman, J. M. *Principles of the Theory of Solids*; Cambridge University Press: Cambridge, 1964.